

**Mainshock Rupture Properties, Aftershock Activities and Remotely Triggered Seismicity
Associated with the 2025 Mw7.7 Sagaing Fault earthquake in Myanmar**

This preprint was submitted to Earthquake Research Advances for peer review on 05/25/2025

Zhigang Peng (zpeng@gatech.edu)¹, Xinglin Lei² (xinglin-lei@ies.ac.cn), Dun Wang³
(wangdun@cug.edu.cn), Xu Si¹ (xsi33@gatech.edu), Phuc Mach¹ (pmach3@gatech.edu), Qiu
Zhong⁴ (qzhong94@gmail.com), Chang Ding¹ (cding64@gatech.edu), Yangfan Deng⁵
(yangfandeng@gig.ac.cn), Min Qin⁶ (yndsn_qm4573@163.com), Suqiu Miao⁶
(miaosql234@163.com)

1. School of Earth and Atmospheric Sciences, Georgia Institute of Technology, Atlanta,
United States, 30332

2. Institute of Geology, China Earthquake Administration, Beijing, China, 100029

3. Chinese University of Geosciences, Wuhan, Hubei, China, 430074

4. Guangdong Earthquake Agency, Guangzhou, China, 510070

5. Guangzhou Institute of Geochemistry, Chinese Academy of Sciences, Guangzhou, China,
510640

6. Yunnan Earthquake Agency, Kunming, China, 650224

Abstract A devastating Mw 7.7 earthquake struck near Mandalay, Myanmar, on March 28, 2025, causing extensive damage and casualties across Myanmar and neighboring regions. The 2025 event occurred in a well-recognized seismic gap along the Sagaing Fault. Here we present preliminary results on the mainshock rupture properties based on back-projection of teleseismic P waves and early aftershock locations, analysis of near-field seismic recordings, and remotely triggered seismicity following the Mw7.7 mainshock. We find that the ~500 km mainshock rupture can be revealed by both rapid back-projection of teleseismic P waves from multiple broadband arrays and early aftershock locations within about 3 hours from the Thai Meteorological Department (TMD) catalog. The rupture speed went supershear in the southward propagation after the initial bi-lateral sub-shear ruptures, as expected for large strike-slip earthquakes of such sizes. In addition, aftershocks from the regional TMD catalog appear to be located mostly to the east of the mainshock rupture. While we cannot completely rule out mislocations from the one-sided station distribution, these off-fault seismicity could also be explained by reactivations of subsidiary faults within the Shan Plateau. Although no immediate foreshocks were found from several nearby stations, we show that the mainshock likely started with a relatively small-magnitude event, likely to the east of the Sagaing Fault. The mainshock also occurred when the tidal stresses reached its maximum on the right-lateral strike-slip fault, indicating that the timing of the mainshock is modulated by the solid earth tides. We also find a significant increase of seismic activity near the Thailand/Myanmar border, in multiple (geothermally active) regions of Yunnan province in Southwest China, as well as the Xingfengjian reservoir in the Guangdong province in South China. Because static stress changes from the mainshock are small but negative near the Thailand/Myanmar border, the occurrence of microseismicity in this and other regions can be mainly explained by remote triggering from dynamic stress changes of the mainshock rupture. Our analyses demonstrate the importance of rapid analysis on openly available seismic data and catalog to better understand the rupture properties and triggered seismicity following large earthquakes.

Major points:

1. The mainshock rupture is supershear with surface rupture length of more than 500 km, resulting in one of the longest strike-slip rupture ever recorded.
2. This event triggered a widespread increase of microseismicity in Southeast Asia, some in the stress shadow casted by the mainshock.
3. The eastern side of the Sagaing Fault possesses a more complex secondary faults governing aftershock activity and possible the initial mainshock rupture.

Key Words: Sagaing Fault, 2025 Myanmar Earthquake, Supershear Rupture, Remote Triggering, Fault Zone Head Waves

1. Introduction

On March 28th, 2025, a moment magnitude (M_w 7.7) earthquake nucleated near Mandalay, the second largest city in Myanmar. The mainshock (termed the Sagaing Fault earthquake in this study) propagated predominately along the Sagaing Fault to the south for about 100 s (Hubbard and Bradley, 2025; Wei et al., 2025; Xu et al., 2025), resulting in significant damages and casualties in Myanmar and neighboring countries such as Thailand and China (Shahzada et al., 2025). The Sagaing Fault is a major ~1400-km-long fault, which accommodates the right-lateral motions between the India-Australia and the Eurasian plates (Tun and Watkinson, 2017). It connects the divergent plate boundaries in the Andaman Sea and the active collision fronts near the Eastern Himalayan Syntax (EHS) in the Tibetan Plateau and hosted multiple $M_w \geq 6$ earthquakes over the past centuries (Wang et al., 2014).

This $M_{7.7}$ event is the largest strike-slip earthquake ever occurred in this region in the past 100 years. While initial finite-fault waveform modeling from the USGS indicated a mainshock rupture length of around 250 km (Hubbard and Bradley, 2025; Cai et al., 2025), subsequent analysis (Bradley and Hubbard, 2025; Wei et al., 2025; Xu et al., 2025; Inoue et al., 2025; Zhao et al., 2025) based on aftershocks from regional earthquake catalogs, back-projection of teleseismic P waves, sub-event analysis, and InSAR data and other remote sensing analysis (https://www.eorc.jaxa.jp/ALOS/jp/library/disaster/dis_myanmar_earthquake_20250409_j.htm) all suggested a much longer surface rupture of about 500 km. Long-period coda wave analysis revealed that the moment magnitude M_w of this event is 7.86 (Li and Song, 2025), consistent with its ultra-long rupture. Here we use the $M_w=7.7$ determined by the USGS for the rest paper.

Resolving the rupture length shortly after a large earthquake like this event helps to determine the places with the strongest shaking (Wald et al., 2022) and subsequent rescue efforts. In addition, it provides robust input for subsequent analysis of the unbroken segment and future seismic hazard in the surrounding region (Toda and Stein, 2025; Li et al., 2025). In this article, we present additional evidence for a simple and long surface rupture, including its supershear rupture properties, which is expected for large strike-slip earthquakes (Robinson et al., 2010; Wang et al., 2016b; Ren et al., 2024). In addition, we include preliminary analysis on the aftershock distributions, Coulomb stress changes due the mainshock, tidal modulations of the mainshock occurrence times, beginning of the mainshock ruptures and widespread remote triggering in South and Southeast Asia following the mainshock.

2. Tectonic Background

While the central section of the Sagaing Fault that hosted the recent $M_{7.7}$ earthquake is relatively simple, the tectonic environment in a broader context is rather complex (Figure 1a). The India-Australia plate moves northward to collide with the Eurasia plate, creating the Himalayan Mountain Front and the Tibetan plateau (Yin and Harrison, 2000). At its eastern edge of the plate boundary, motion between the two plates is highly oblique, which is accommodated by the Indo-Burma subduction zone (IBSZ), the Sagaing Fault and other strike-slip faults in the Indo-Burma area (Figure 1a). Further south, such an oblique motion is accommodated by the Sumatra-Andaman subduction zone and the Great Sumatran fault (McCaffrey, 2009). In between these active faults lies the Burma microplate, which is a small tectonic plate located between the Indian Plate and the Sunda Plate, accommodating complex interactions such as oblique subduction, strike-slip motion, and back-arc deformation in the eastern Indian Ocean region (Gahalaut and Gahalaut, 2007).

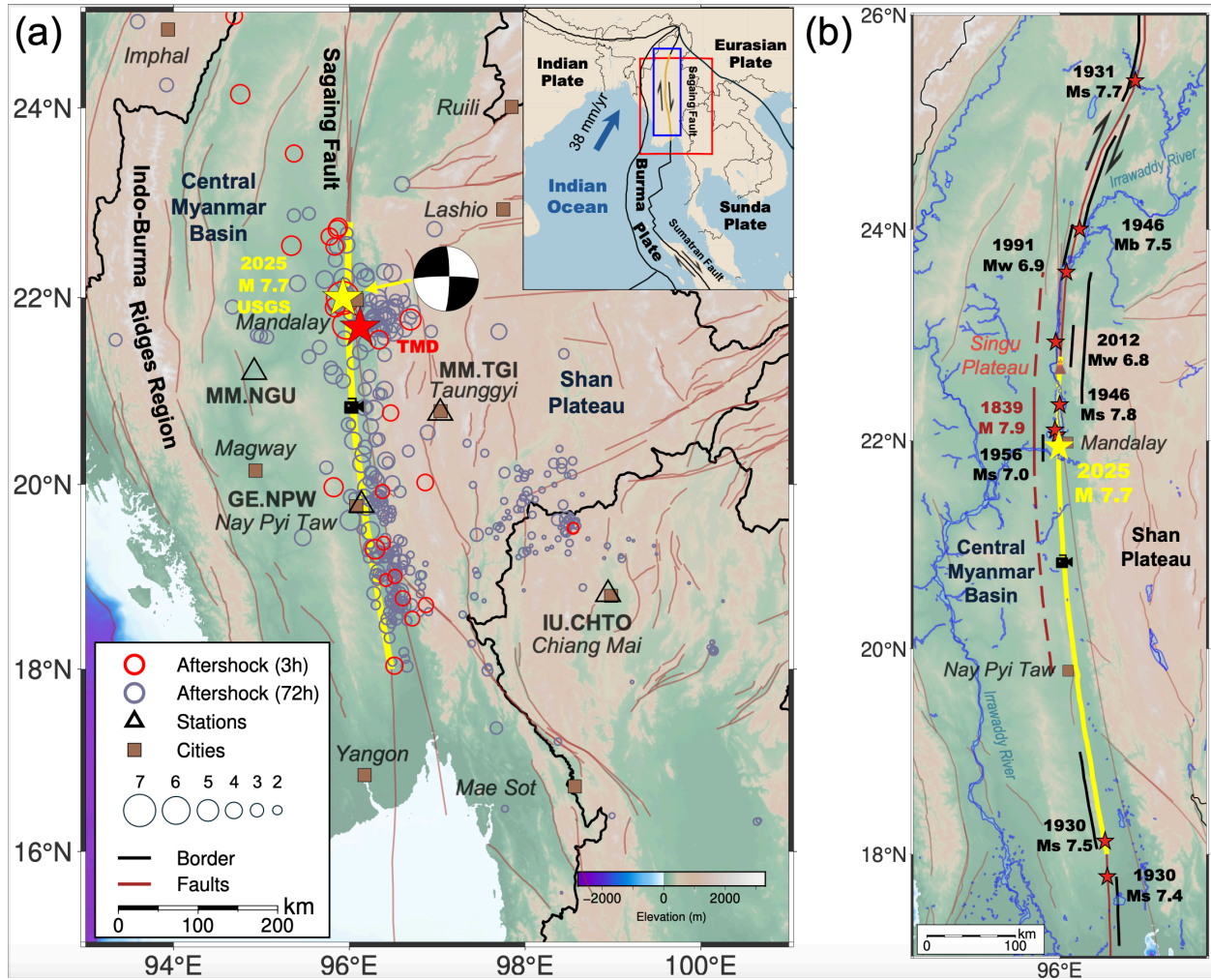


Figure 1. The 2025 Mw 7.7 earthquake hypocenter near Mandalay, Myanmar, seismic activity following the mainshock and its tectonic setting. (a) Map showing aftershock distribution within 3 and 72 hours following the 2025 Mw 7.7 mainshock, along with seismic stations (triangles) and major cities (brown squares). The yellow and red stars mark the mainshock hypocenters from the USGS and TMD catalogs, respectively. The black camera sign shows the location where a surface rupture video was captured by a security camera (Latour et al., 2025). The inset map displays the regional tectonic setting, including the Eurasian, Indian, Burma, and Sunda plates, and other major faults. (b) Historical large earthquakes ($M \geq 6.8$) along the Sagaing Fault. The ~500-km-long rupture zone of the 2025 event is marked as yellow rectangle. Each historical event's rupture length is shown as an orange rectangle. Hypocenter locations and rupture lengths are based on Xiong et al. (2017) and Hubbard & Bradley (2025).

The Sagaing Fault is the dominant tectonic feature in Myanmar (Tun and Watkinson, 2017), which separates the Central Myanmar Basin (CMB) to the west, and the Shan Plateau to the east (Figure 1). Further to the west of the CMB lies the Indo-Burma Mountain Range (IBMR), which is generally interpreted as the accretionary wedge due to the IBSZ. The IBMR (and to a less degree the Sagaing Fault) shows a convex shape westward towards the Bengal basin, which has been interpreted as a combined effects of the buttressing to the north by the

Shillong Plateau and the EHS (Nielsen et al., 2004), and the westward crustal flow related to the Tibet Plateau collapse (Rangin et al., 2013). Geodetic measurements revealed ~18-22 mm/year of dextral strike-slip motion along the Sagaing Fault (Wang et al., 2014; Mallick et al., 2019; Lindsay et al., 2023). Stress inversions from focal mechanisms of moderate-size earthquakes in this region revealed that the maximum horizontal compressive stress direction is in the NE-SW (Hu et al., 2017; Timsina et al., 2024).

The Sagaing Fault has long been recognized as one of 11 “earthquake fault superhighways”, where continental strike-slip faults with very long and straight segments (Robinson et al., 2010). It passed near several major cities (e.g., Mandalay, the capital Naypyidaw, and Yangon), and has hosted more than 10 M6+ earthquakes in the past centuries (Figure 1b). Among them, the 1839 Ava earthquake (M7.9-8.3) likely ruptured a similar segment when comparing with the most recent M7.7 event (Wang et al., 2014; Hubbard and Bradley, 2025). The northern end of the M7.7 event (~22.5 deg) appeared to stop at the Singu Plateau (also known as Letha Taung), a small basaltic plateau that are offset by the Sagaing Fault (Tun and Watkinson, 2017). It also partially overlaps with the southern end of the 2012 M6.8 Thabeikkyin earthquake (Wei et al., 2025). The southern end of the M7.7 event (~18 deg) appears to be close to or overlaps with the M7.3 earthquake in 1930 (Wang et al., 2014; Hubbard and Bradley, 2025; Wei et al., 2025). Coulomb stress transfer calculations from 10 M>6.5 earthquakes along the Sagaing Fault (Xiong et al., 2017) also showed that most subsequent events occurred in the positive stress increase section following the previous events, and the central and southern section is due for a large earthquake. In this perspective, this M7.7 event is well expected (Hubbard and Bradley, 2025), because it occurred in a *seismic gap* (Mogi, 1979; Jackson and Kagan, 2011; Kagan et al., 2012) where significant slip of ~4 m (as expected from the mean slip rate) has accumulated in the past few centuries without any major earthquakes releasing the strain.

3. Mainshock Rupture Properties from Back-projection Analysis

We apply the back-projection method (Wang et al., 2011; Wang et al., 2016a) to image the rupture process of the 2025 Myanmar earthquake using teleseismic data recorded by regional arrays in Europe, Alaska, and Australia (Figure 2a). These three arrays are located to the northwest, northeast, and southeast of the epicenter, respectively, with epicentral distances ranging from 30° to 90°, which is the optimal range for teleseismic P-wave back-projection (Kiser and Ishii, 2017).

The back-projection results from the three arrays consistently show that the primary fault involved in this earthquake was the Sagaing Fault. The rupture started near the epicenter and initially propagated northward over approximately 100 km (Figure 2b). It then progressed southward, releasing most high-frequency energy in that direction. The southward rupture extended for at least 300 km, and the total rupture duration was approximately 70–90 seconds, with minor variations among arrays. This relatively long rupture extent significantly exceeds the empirical expectation of no more than 250 km for a Mw7.7 event (Wells and Coppersmith, 1994; Bradley and Hubbard, 2025b). Although the average rupture velocity is approximately 3–4 km/s, Figure 2b-d clearly shows that portions of the southern segments with the rupture speed exceeding 5 km/s. These preliminary findings are generally consistent with the sub-event inversion analysis (Bradley and Hubbard, 2025b) and other back-projection results (Wei et al., 2025; Xu et al., 2025). Together these studies provide strong evidence for the occurrence of

southward-propagating supershear rupture. This observation is also consistent with previous studies suggesting that supershear rupture is commonly associated with strike-slip earthquakes (Wang et al., 2016b).

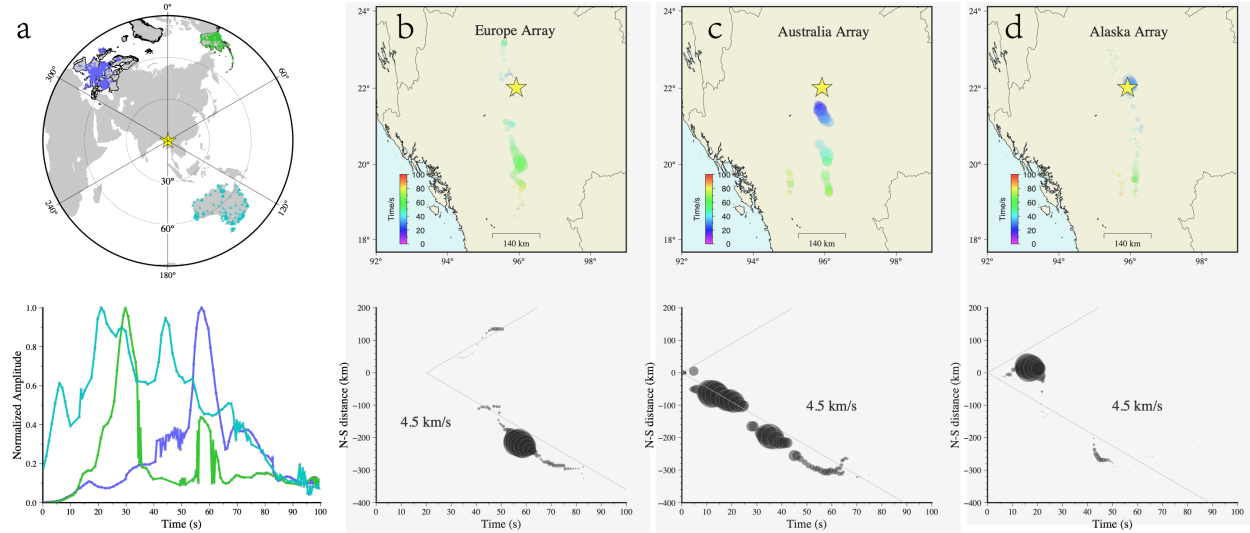


Figure 2. Teleseismic P-wave back-projection of the 2025 Sagaing Fault earthquake. (a) (Top) Locations of the Europe (EU), Australia (AU) and Alaska (AL) regional seismic arrays. (Bottom) The normalized amplitudes as a function of time for three arrays. (b) Top: spatial distribution, timing, and amplitude of maximum-correlation back-projection beams at 1-second intervals using the Europe array for the 2025 Sagaing Fault earthquake. Bottom: time–distance plot showing the rupture propagation speed of the maximum energy point over time. The yellow star indicates the mainshock epicenter. (c) and (d) Same as (b), but using the Australia and Alaska arrays, respectively.

4. Early Aftershock Distributions

Next, we constrain the mainshock rupture length from the locations of early aftershocks following the M7.7 mainshock. Aftershock rates typically decay with time since the mainshock following the Omori’s law (Utsu et al., 1995), while the aftershock area expand from the mainshock rupture region, generally following logarithmic time since the mainshock (Peng and Zhao, 2009). Hence, the best time to use aftershock location to reflect the mainshock rupture area would be immediately following the mainshock (i.e., hours to one day) (Henry and Das, 2001). However, global seismic catalogs such as the USGS NEIC or the Global CMT catalogs typically have a relatively high magnitude of completeness (M_c) of about 5, especially right after the mainshock (Iwata, 2008). Hence, the early aftershock numbers are typically not enough to provide a reliable constraint on the mainshock rupture area. On the other hand, regional earthquake catalogs contain more smaller events that can be used to delineate the aftershock zone and the mainshock rupture area (Lengline et al., 2012; Bradley and Hubbard, 2025a).

We collect regional and global earthquake catalogs for this region since March 2025 and merge them into one uniform catalog (Table S1). Among them, the Thai Meteorological Department (TMD) earthquake catalog contains the greatest number of events and is used primarily for the rest of the analysis. Because the Thailand catalog is built from seismic stations primarily in Thailand, their location uncertainties are relatively high. Hence, we select

earthquakes within 50 km of the N-S striking Sagaing Fault (centered at the mainshock location as determined by the USGS). The lower-magnitude cut-off decays with time since the mainshock, reflecting that a significant fraction of aftershocks is not detected right following the mainshock (Kagan, 2004). Within the first 3 hours following the mainshock, we find 17 aftershocks along the N-S striking Sagaing Fault, which clearly define a ~500-km-long zone that can be interpreted as the mainshock rupture zone (Figure 3b). We note a relative lack of early aftershocks between 19.5°N and 21.5°N. Although aftershocks occurred slightly later in this region, its density is not smaller than the sections above and below (Figure 3b). In addition, we identify a significant number of events near the border between Myanmar and Thailand (Figure 1). These earthquakes are likely dynamically triggered seismicity and are analyzed further in the following section.

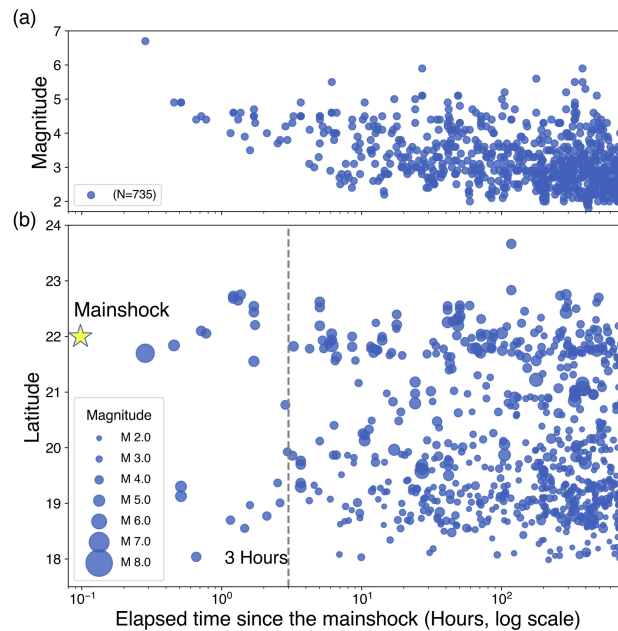


Figure 3. Aftershocks within one month following the mainshock. (a) Magnitude versus elapsed time (in hours, log scale), showing temporal evolution of the aftershock. (b) Latitude versus elapsed time (in hours, log scale). Circle sizes are scaled by magnitude, as shown in the legend. A vertical dashed line at 3 hours highlights the early aftershock.

In addition to the N-S along-strike distribution, we also note that aftershocks are distributed in the E-W direction for up to 100 km long (Figure 1a). For example, a significant portion of aftershocks near the epicenter (around 22°N) occurred to the east of the Sagaing Fault. In addition, aftershocks south of the epicenter and Naypyidaw (around 20°N) are relatively sparse, which is also shown in the along-strike versus log-time plot since the mainshock plot (Figure 3b). We also generate a zoom-in plot to show the aftershock distribution on top of pre-existing faults south of the mainshock epicenter (Figure 4a). Notes that the mainshock source fault trace in the plot is closely aligned with JAXA's InSAR data (https://www.eorc.jaxa.jp/ALOS/jp/library/disaster/dis_myanmar_earthquake_20250409_j.htm) and thus very precise. Although some aftershocks occurred to the west of the Sagaing Fault in the CMB, majority of them occurred within the Shan Plateau to east of the Sagaing Fault (Figure 4b). We also plot the aftershocks located by the USGS and those by the TMD. As expected, aftershocks in the TMD catalog were systematically located to the Shan Plateau side, and the

mean/median difference in the fault-normal distance is about 25 km. Hence, at least some of the aftershock shift to the Shan Plateau can be explained by such a systematic bias in the aftershock locations in the TMD catalog.

In addition to directly using the regional earthquake catalogs, we also examine the continuous waveforms for the 4 nearest stations within 500 km of the mainshock epicenter (Figure 1a). These include two stations in the Myanmar's national seismic network (netcode: MM) (Thiam et al., 2017), one station GE.NPW operated by the the GFZ Helmholtz Center for Geosciences (GFZ) (Lai et al., 2025), and one Global Seismic Network (GSN) station IU.CHTO. We apply a band-pass-filter of 5-15 Hz to suppress the coda of the mainshock and large aftershocks, followed by taking a smooth function with a half-width of 100 point and finally taking the log10 (Peng et al., 2006, 2025). In addition to those 4 events (including the M7.7 mainshock) listed in the regional and global catalogs within the first hour of the mainshock, many high-frequency bursts can be visually identified (Figure 5). These events either occurred along the Sagaing Fault as early aftershocks, or they may occur off the Sagaing Fault as triggered seismicity.

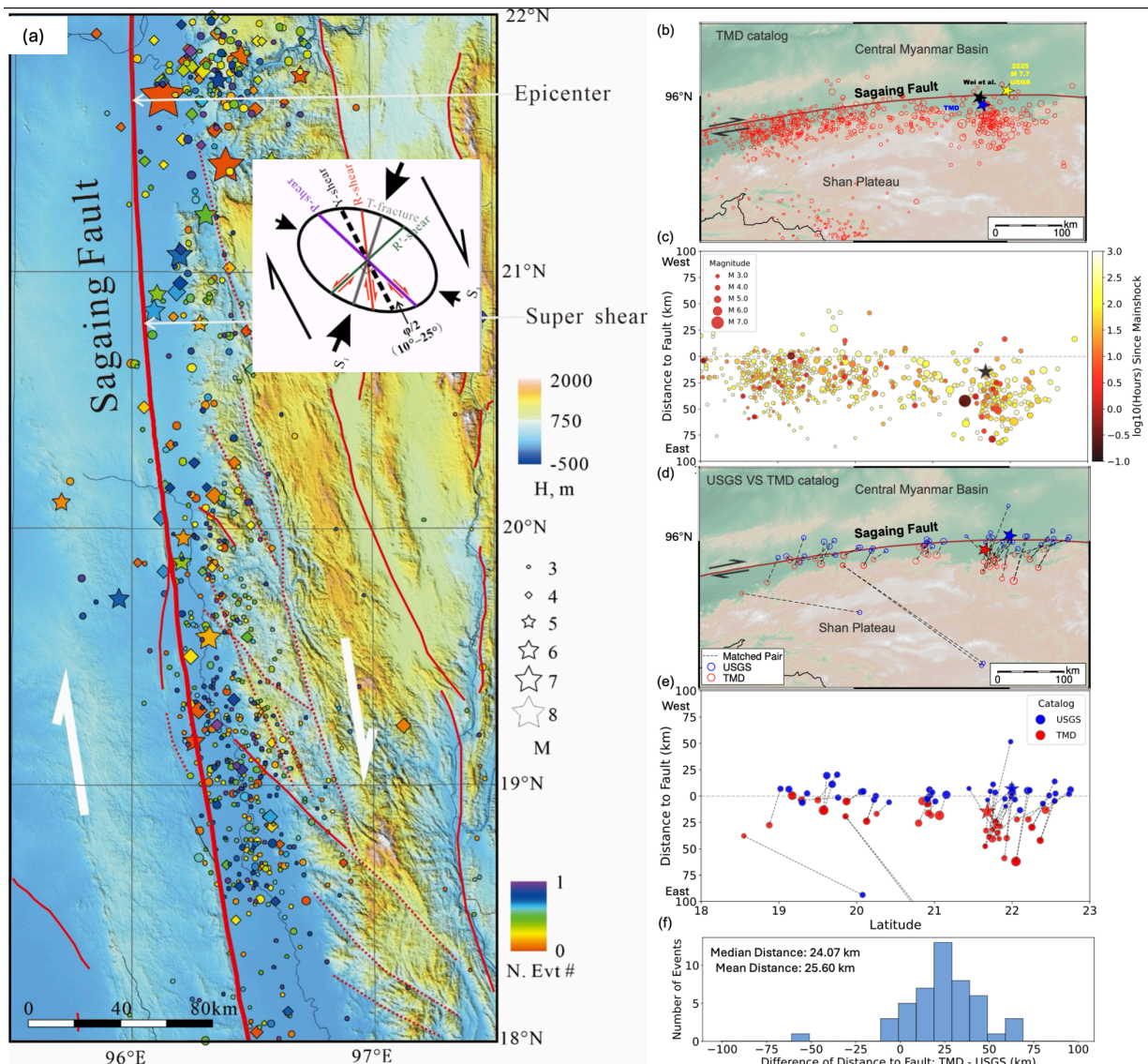


Figure 4. Spatial distribution and catalog comparison of aftershocks following the 2025 M7.7 mainshock. (a) A zoom-in plot showing aftershock locations listed in the TMD catalog relative to the mainshock rupture trace (thick red line). The thin red solid and dashed lines mark the local fault traces and those visually identified based on geomorphic features. (b) Epicentral distribution of the TMD catalog, with events sized by magnitude. The Sagaing Fault trace and regional tectonic features such as the Central Myanmar Basin and Shan Plateau are annotated. The yellow star marks the USGS mainshock location, the black star shows the location from Wei et al. (2025), and the blue star indicates the TMD mainshock location. (c) Distance of aftershocks to the Sagaing Fault as a function of latitude, where the vertical axis represents the perpendicular distance mapped onto the fault trace. The spatial distribution of seismicity across the fault is evident, with temporal evolution illustrated by the color scale (logarithmic hours since the mainshock). (d) Comparison of matched events between the USGS (blue) and TMD (red) catalogs, plotted by latitude (horizontal axis) and longitude (vertical axis). Dashed lines connect each matched pair, illustrating differences in their locations and their respective distances to the Sagaing Fault. (e) Distance-to-fault plotted against latitude for all matched events. USGS (blue) and TMD (red) locations are shown for each pair, with vertical dashed lines connecting the corresponding points. (f) Histogram of differences in fault-perpendicular distance between matched TMD and USGS events. The median and mean offsets are calculated as the distance from each TMD event to the fault minus that of its USGS counterpart.

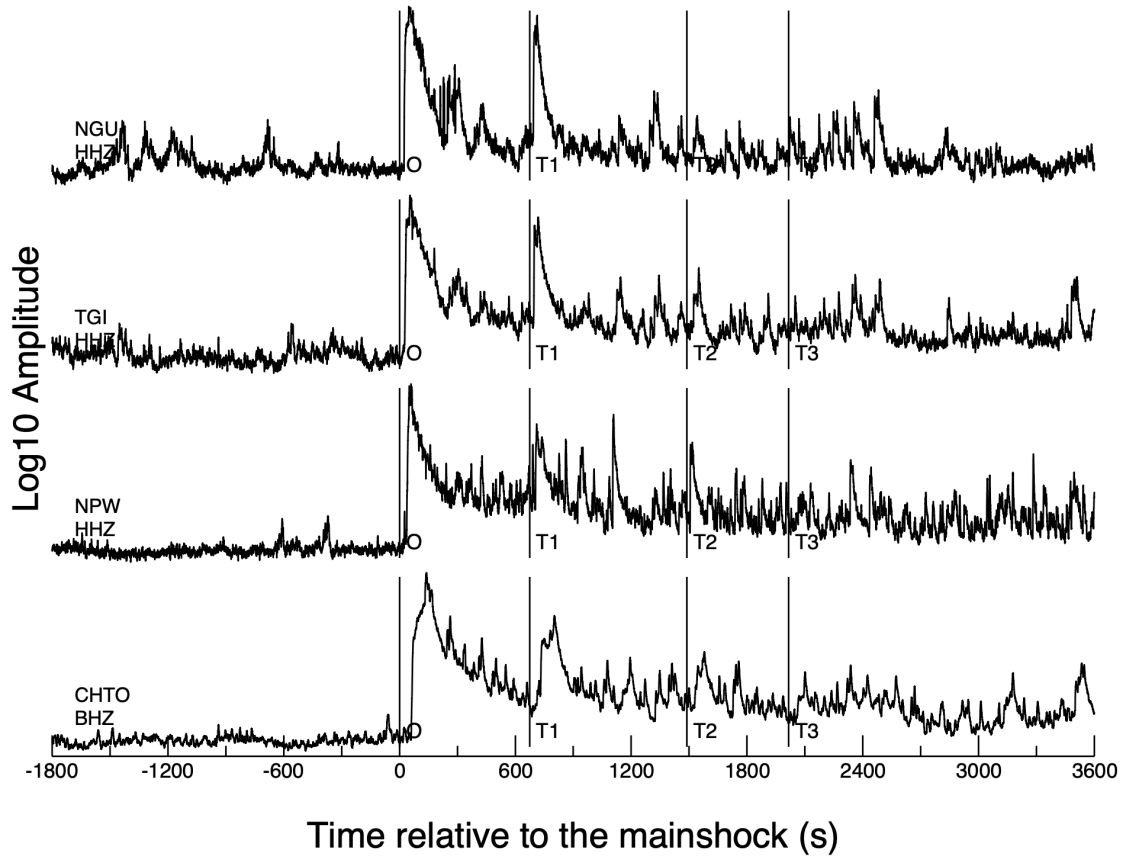


Figure 5. 5-15 Hz band-pass-filtered envelope functions of waveforms recorded over a 1.5-hour period around the M7.7 mainshock by the vertical components of 4 nearest stations. The time

flags (0, T1, T2 and T3) mark the origin time of the mainshock, the M6.7 aftershock and two additional aftershocks recorded in the TMD catalog.

5. Seismicity Before the Mainshock and Mainshock Waveforms

In this section, we focus on the seismic activity in the last few weeks before the M7.7 mainshock as well as the first few seconds of the mainshock ruptures. By examining both the regional Thailand earthquake catalog within one year of the mainshock and the continuous waveforms in the last day, we find no single event occurring within 50 km of the mainshock epicenter in the last three months (Figure S1). Hence, similar to the 2023 M7.8 Pazarcik event in the Kahramanmaraş Earthquake Sequence (Kwiatek et al., 2023), no immediate foreshock was identified from existing catalogs. It is possible that smaller events may have occurred in this region, but it requires a more systematic analysis that is beyond the scope of this manuscript.

A close examination of the mainshock waveforms at the nearest three stations reveal additional details on the initial and mainshock rupture phases (Figure 6a). Here we do not apply any filters or instrument corrections to the broadband recordings but only plot them in different amplitude and time scales. We also include the velocity seismogram integrated from the acceleration recordings (HN channels) at station GE.NPW that is about 2.6 km west of the M7.7 mainshock surface rupture zone (Lai et al., 2025). While it is still possible to identify the initial S waves at stations MM.NGU and MM.TGI before the broadband recordings went off-scale, the broadband recordings at station GE.NPW went off-scale much earlier than the predicted S arrivals (Figure 6a). However, the on-scale velocity seismograms from integrating the acceleration shows a strong pulse arriving at 48.5 and 51 s, with the peak value of 1.64 m/s at ~50 s. Here we use the reference origin time of 2025/03/28 06:20:55.209 UTC (Wei et al., 2025). If we also use their mainshock location (21.641°N, 96.022°E, 10 km depth), the corresponding hypocentral distance and rupture speed would be 206.6 km and 4.13 km/s, respectively. This observation again confirm that the southward rupture propagation is primarily supershear (Lai et al., 2025; Wei et al., 2025; Xu et al., 2025).

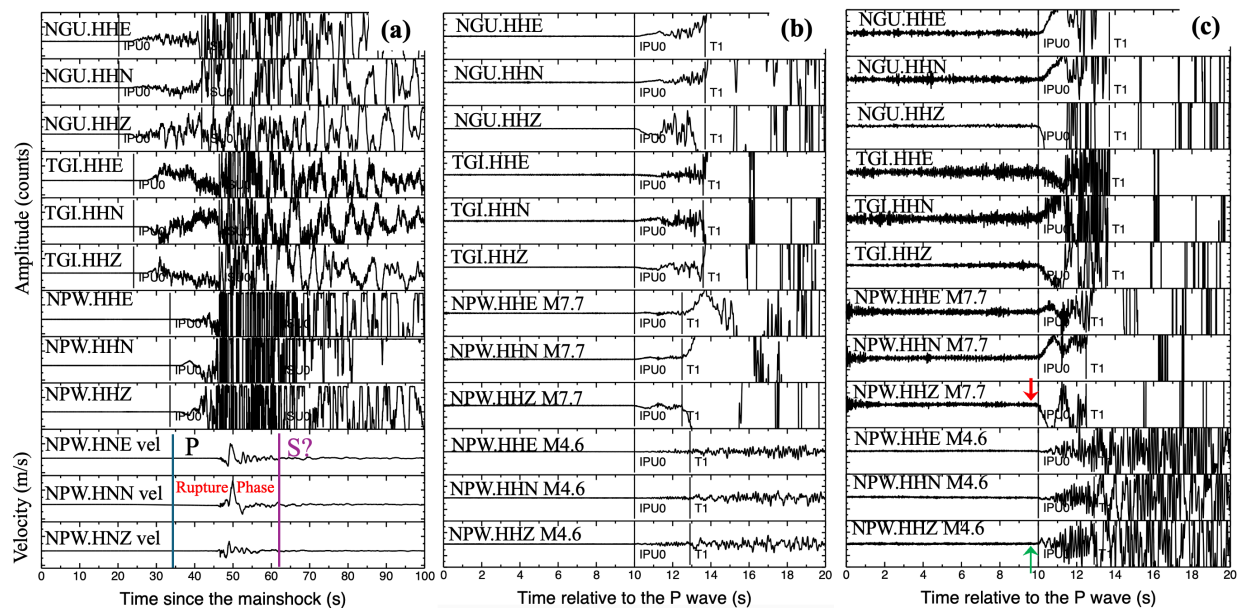


Figure 6. (a) A comparison of the first 100 s of the M7.7 mainshock recording at the three broadband stations. The bottom three traces are velocity seismogram integrated from the strong-motion recordings at station GE.NPW ~ 2.6 km west of the mainshock rupture zone. The P and S lines mark the expected P and S arrivals at this station. (b) A Zoom-in plot showing a comparison between the P waves of the M7.7 mainshock with respect to a M4.6 aftershock close to the relocated mainshock hypocenter on 2025/04/04. (c) A further zoom-in plot showing the initial P wave polarity. Note that the polarity of the M7.7 mainshock and the M4.6 aftershock at station GE.NPW is flipped.

Figure 6b and 6c also show the zoom-in plots of the P waves at three stations, including a comparison with the P wave at the same GE.NPW station for a M4.6 aftershock on 2025-04-04 15:25:24 UTC (10 km depth, 21.5621°N). A strong phase in the same direction is shown at stations MM.NGU, MM.TGI and GE.NPW after ~ 3.7 , ~ 3.6 and ~ 2.5 s of the initial P waves, respectively. Because of the increasing distances from the initial hypocenter to these stations, we expect to see an increasing time separation of we interpret these phases as the Pn and Pg waves. Hence, we argue that the second strong phase is likely from a second stronger sub-event following the initial P wave. Because of the shorter time separation at station GE.NPW, we expect that the second source is closer to this station, indicating a southward propagation of the rupture. Note that station GE.NPW has about 0.78 s of timing drift at the time of the mainshock (Lai et al., 2025). However, here we use only the relative time difference between these phases and hence it is not affected by such a timing issue. Finally, we note that the initial polarity of the M7.7 mainshock at station GE.NPW is down, while the initial polarity of the M4.6 aftershock is up (Figure 6). The expected polarity for a right-lateral strike-slip event at station GE.NPW is down for a homogenous medium. However, most of the aftershocks north of this station shows a weak upward motion followed by a strong downward motion (Figure 7). The initial phases from most aftershocks can be interpreted as fault zone head waves refracted along a bi-lateral fault interface (Ben-Zion and Malin, 1991; Zhao and Peng, 2008), which would be recorded as the first arrivals for stations on the slower side of the fault (i.e., the Central Myanmar Basin in this case). If this interpretation is correct for most aftershocks, then the initial mainshock is either not on the Sagaing Fault, or its focal mechanism is not purely strike-slip fault.

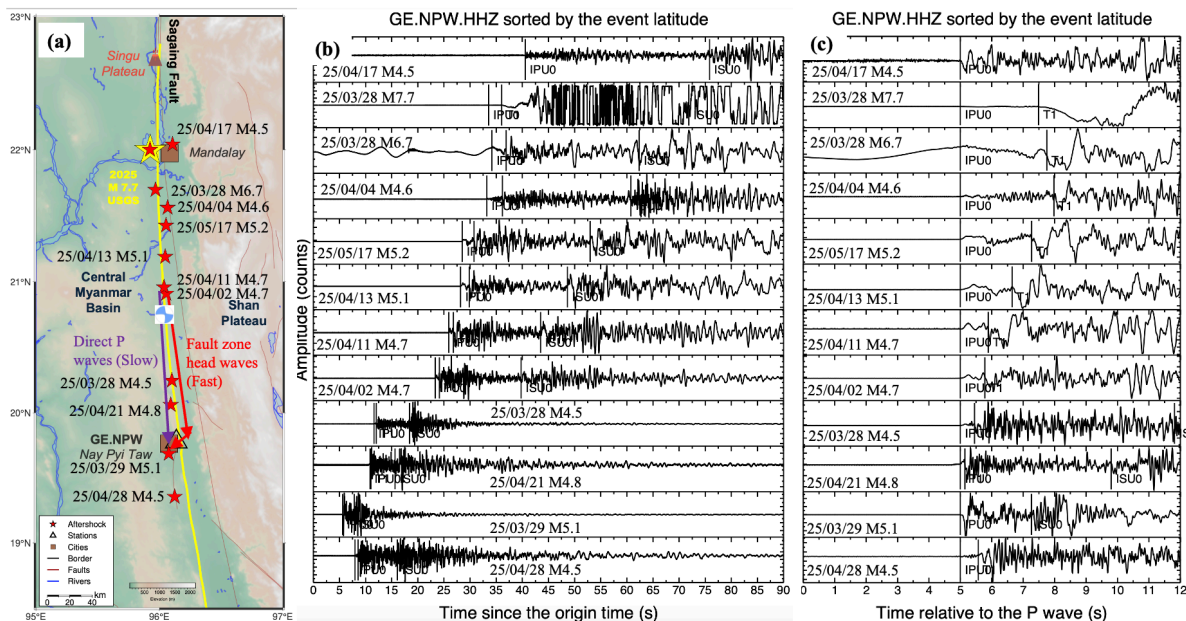


Figure 7. (a) A map showing the locations of the M7.7 mainshock and other 11 aftershocks. The red and purple arrows mark the expected ray paths for fault zone head waves along the faster side (Shan Plateau), and the direct P wave along the slower side (Central Myanmar Basin). (b) Vertical-component seismograms recorded at station GE.NPW sorted by the event latitudes. The initial weak P waves, abrupt secondary arrivals, and the S waves are marked. (c) Same plot as (b) except that all traces are aligned by the initial P waves.

6. Tidal Triggering of the Mainshock

In this section we evaluate whether solid Earth tides have played any role in the eventual timing of the mainshock, which has been a subject of debates for decades (Ide et al., 2016; Hough, 2018; Bradley and Hubbard, 2024). We calculate the strain tensors generated by solid Earth tides and ocean tides using the program GOTIC2 (Matsumoto et al., 2001), which employs the 1066A elastic Earth model (Dziewonski et al., 1975). To enhance the accuracy of ocean tidal loading effects, GOTIC2 incorporates the improved ocean tide model NA0.99b, which was widely used in previous studies on tidal triggering of earthquakes (Tanaka et al., 2012). The computed strain is then converted to stress using a bulk modulus of ~ 42 GPa and a shear modulus of ~ 28 GPa, derived from the average P-wave and S-wave velocities and density in the 3–15 km depth range of the 1066A model. Tidal strains are independent of fault orientation. However, for faults with specified strike, dip, rake, and frictional coefficient, we further calculate the normal stress, shear stress, and Coulomb Failure Stress (CFS) to evaluate tidal response.

Since the mainshock occurred just before the new moon (03/29/2025), we first calculate the tidal strains and stresses from long-period waves on a fault with orientation (strike, dip, rake) = $(358^\circ, 82^\circ, -175^\circ)$, corresponding to the USGS CMT solution. The mainshock timing coincides with peaks in volumetric strain, and CFS (Figure 8a). Notably, the amplitudes of long-period waves modulate those of diurnal and semi-diurnal tidal waves. We further computed tidal stresses for all tidal components (long-period, diurnal, and semi-diurnal) over time spans of 10 days. The results reveal that both the mainshock and some large aftershocks ($M \geq 5.0$) coincide with peaks in CFS or shear stress (Figure 8b). These findings suggest that tidal loading likely played a role in modulating the timing of the mainshock and some large aftershocks, consistent with results from several recent moderate-size earthquakes (Ide et al., 2016; Chuang et al., 2023).

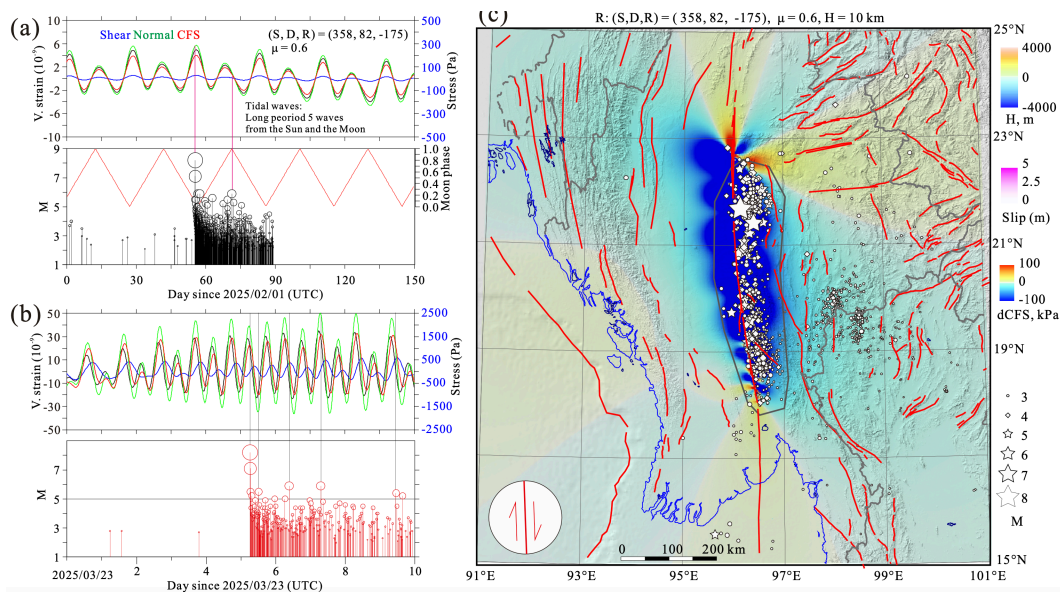


Figure 8. Comparison of tidal strains/stresses and earthquake occurrence times. (a) Long-period tidal wave components and M-T plot. (b) Full tidal wave spectrum (including diurnal, semi-diurnal, and long-period components) and M-T plot for 10 days since March 23, 2025. (c) Map view of active faults and earthquake distribution overlying on change of Coulomb Failure Stress (dCFS) from the 2025 M7.7 mainshock for faults parallel with the Sagaing Fault; events within the outlined polygon are analyzed in panels (a)-(b).

7. Coulomb Stress Changes from the Mainshock

Large earthquakes are expected to transfer static stresses to nearby faults and change the occurrence of future earthquakes on those faults (Stein, 1999). Several recent studies have examined how previous earthquakes loaded the central and southern section of the Sagaing Fault before the M7.7 mainshock (Xiong et al., 2017). In addition, rapid analyses also revealed how static Coulomb stress changes from the 2025 M7.7 mainshock would affect earthquake occurrences on faults parallel to the Sagaing Fault (Toda and Stein, 2025) and other faults in the neighboring Yunnan province in Southeast China (Li et al., 2025). Here we adapt the coseismic fault slip model published by the USGS and the aforementioned crustal model for tidal stress calculation to compute the coseismic static stress changes of the M7.7 Sagaing Fault earthquake on surrounding areas. For comparison, we first calculate the Coulomb stress changes on receiver faults parallel to the Sagaing Fault. The results are shown in Figure 8c with superimposed aftershock distributions from the TMD catalog. This figure reveals that numerous aftershocks along the mainshock rupture segment are distributed within stress shadow zones. As noted before, most aftershocks occurred in the eastern side of the Sagaing Fault, which features a relatively complex secondary fault network, and appears to dominantly control aftershock occurrence. Analysis of aftershock clustering characteristics and known fault geometries suggests that faults striking N30°W (Figure 4) may constitute one of the seismogenic structures for these aftershocks, with corresponding Coulomb stress changes illustrated in Figure 9a. Due to fault bend and heterogeneous coseismic slip, some stress-enhanced areas emerge in both sides of Sagaing Fault zone. Given the substantial uncertainties remaining in the mainshock fault model and hypocenter locations, we conclude preliminarily that the eastern side of the Sagaing Fault possesses a more complex secondary fault network than the western block, which governs most aftershock activity.

Figure 9b shows a similar calculation but for receiver faults that are nearly E-W trending. Those faults are distributed mainly along the Myanmar-China border. As expected, the M7.7 mainshock rupture casted a positive stress changes (on the order of a few to a few tens of Kpas) to those faults north of 21°N. Further to the south, most of the E-W trending faults would be in the stress shadow, similar to the other two receiver fault geometries (Figure 8b, 9a).

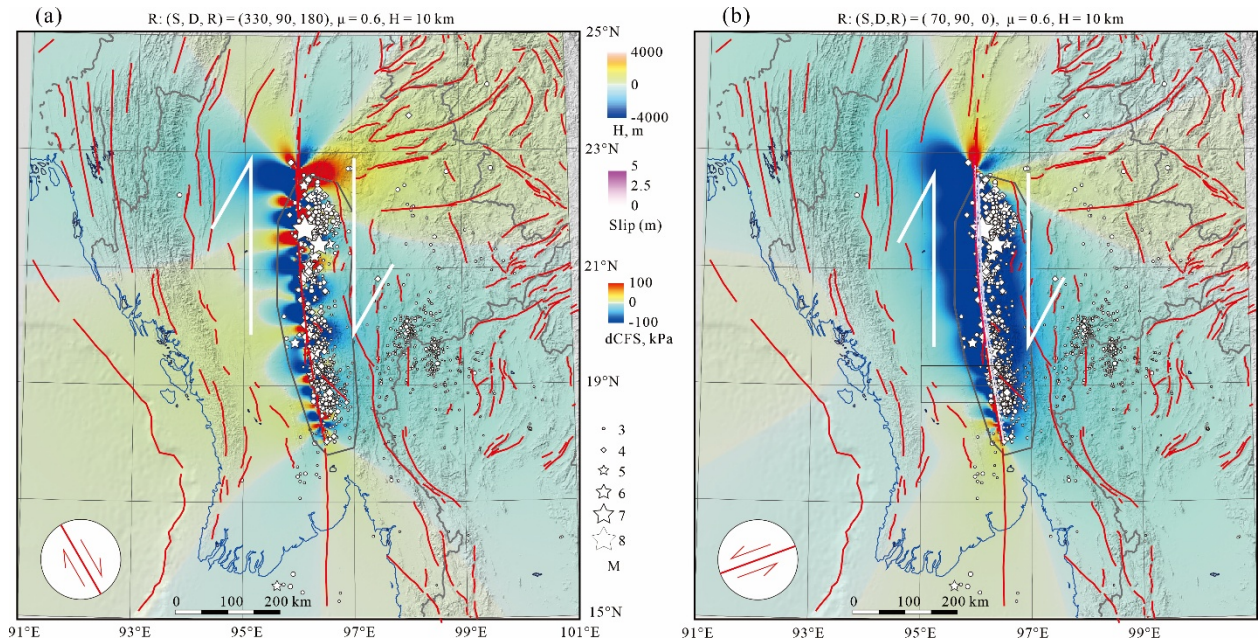


Figure 9. (a) Map view of active faults and earthquake distribution overlying on change of Coulomb Failure Stress (dCFS) from the 2025 M7.7 mainshock for receiver fault of (strike, dip, rake) = (330, 90, 180), frictional coefficient of 0.6, and at a depth of 10 km. (b) The same plot for receiver fault of (strike, dip, rake) = (70, 90, 0), frictional coefficient of 0.6, and at a depth of 10 km.

8. Remotely Triggered Seismicity in Southeast Asia

Large strike-slip earthquakes can generate strong surface waves (especially Love waves) that are capable of triggering both regular microearthquakes and deep tectonic tremor at thousands of kilometers (Prejean et al., 2004; Peng and Chao, 2008; Peng and Gomberg, 2010; Pollitz et al., 2012; Hill and Prejean, 2015; Yao et al., 2024). Hence, we expect that the M7.7 mainshock are also capable of triggering seismic activity well beyond the traditional aftershock zone, which is also known as remotely triggered seismicity. Here we focus primarily on the following three regions (Southeast of Myanmar, Yunnan province in Southeast China and Guangdong province in South China), mainly because of easy access of both regional catalogs and waveform data.

In the southeast of Myanmar lies the Shan Plateau, a topographic high with an average elevation of about 1000 m that extends from Thailand to the Yunnan province, China (Bertrand and Rangan, 2003). Many earthquakes with moment magnitudes larger than 6 have occurred in the past century (Wang et al., 2014), especially the 1912 Ms 7.7 Maymyo earthquake near the Taunggyi city (Crosetto et al., 2019). The recorded events in this region are mainly located near the Kyaukkyan fault, which extends southward to the Mae Ping fault zone running along the Myanmar-Thailand border (Wang et al., 2014). While this region is not well studied in terms of remote dynamic triggering, a Mw 5.8 earthquake near Namzang, Myanmar, occurred 30 min following the 2004 M9.1 Sumatra earthquake, with another Mw 5.1 event happening 4 days after (Ruan, 2007), indicating that this region is susceptible to remote dynamic triggering (Figure 10a). Another group of earthquakes is in northern Thailand, close to the Myanmar border. This region is filled with faults running across major provinces in northern Thailand, including Mae

Hong Son and Chiang Mai. Events in this area are associated with the Mae Hong Son fault and the Mae Tha fault. The Mae Hong Son fault was associated with a Mw 5.6 earthquake that happened in February 1975 near the southern part of the fault (Chansom et al., 2022).

Since most of the Myanmar National Seismic Network's broadband stations are currently inactive, the detection of events in this region largely depends on the seismic stations operated by the TMD, which are deployed in the northern and northwestern parts of Thailand. Figure 10a shows the spatial distribution of events in this study region, 30 days before and after the 2025 M7.7 earthquake. A significant increase in the cumulative number of events is observed after the mainshock (Figure 10c). This suggests that the earthquakes in this specific area of Myanmar and Thailand were remotely triggered immediately by the Mw 7.7 mainshock. Coulomb stress calculations from the previous section (Figures 8c and 9) indicated that static stress changes from the mainshock are negative and on the order of ~ 1 KPa or less in this region. Figure 10b shows first 6000 seconds after the mainshock at the seismic station TM.CMMT in Chiang Mai, Thailand, recording the Mw7.7 mainshock, the largest aftershock of Mw6.7, multiple aftershocks, and a local triggered event Ms3.3 in Mae Hong Son, Thailand. Many high-frequency signals are recorded immediately following the mainshock that were not listed in the TMD catalog. They are likely local seismicity in that region triggered by the M7.7 mainshock. Hence, the observed sudden increase of seismicity in the Shan plateau can be best explained as triggered by dynamic stress changes from the passing waves of the M7.7 mainshock.

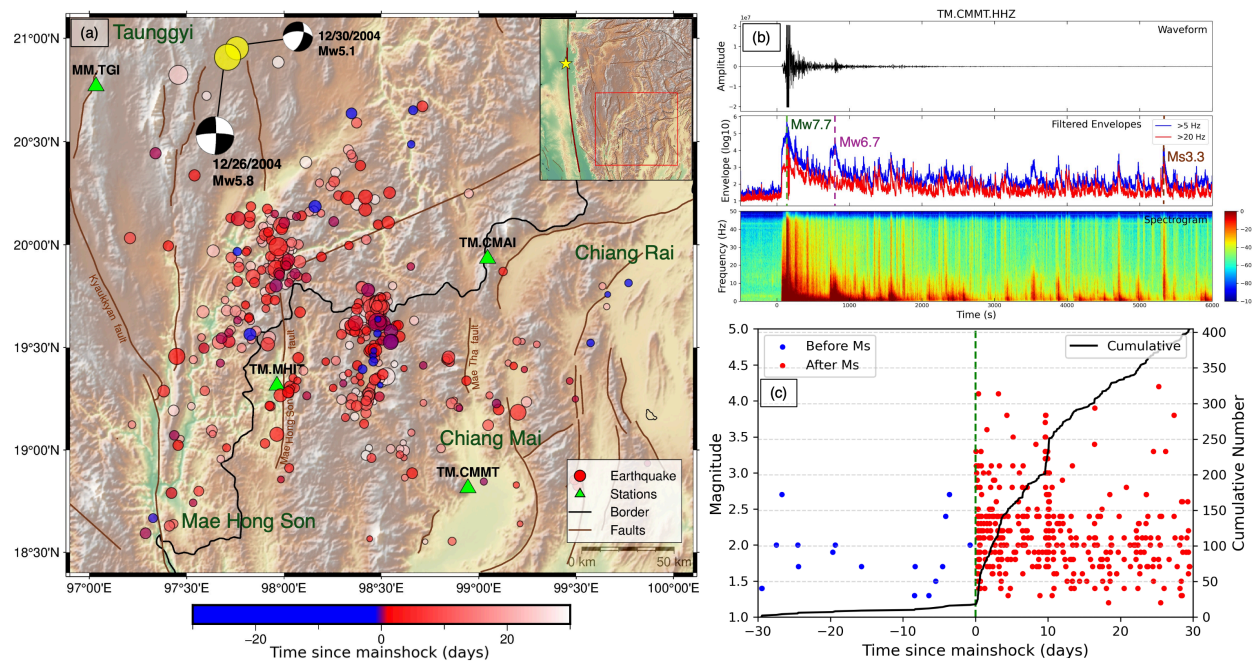


Figure 10. (a) Spatial distribution of earthquakes 10 days before and after the Myanmar earthquake on March 28th, 2025. (b) The log₁₀ envelope function of the vertical component, 5000 seconds after the mainshock, recorded at three broadband stations in Thailand. (c) Earthquake magnitude – time plot for the analyzed region, 10 days before and after the mainshock, with the cumulative number of events calculated.

Yunnan Province, situated on the southeastern margin of the Tibetan Plateau, is a tectonically complex and seismically active region influenced by the ongoing convergence

between the Indian and Eurasian plates. Major fault zones in this area including the Red River Fault Zone (RRFZ), Xiaojiang Fault, and Nujiang Fault, which have hosted frequent moderate-to-strong earthquakes. In addition, previous studies have shown that several faults in Yunnan, including the Tengchong volcanic regions, are prone to dynamic triggering by teleseismic waves from large distant earthquakes (Lei et al., 2011; Li et al., 2019). The triggered seismicity mostly occurred in sites with complex fault geometries or volcanic/geothermal areas, likely due to the presence of high-fluid pressures in these regions.

After the 2025 Mw 7.7 Myanmar mainshock, enhanced seismicity was observed in western and southern Yunnan. As shown in Figure 11a, post-mainshock earthquakes (red circles) cluster around the RRFZ and nearby fault systems. Notably, Figure 11b highlights a group of events that occurred nearly simultaneously with the arrival of the surface waves from the mainshock, strongly suggesting dynamic triggering. This spatiotemporal pattern aligns with observations from previous events such as the 2004 Sumatra and 2012 Indian Ocean earthquakes, which also remotely triggered seismicity in Yunnan (Lei et al., 2011; Li et al., 2019). These results further confirm that faults in Yunnan remain highly responsive to dynamic stress perturbations and represent an important natural laboratory for studying remote triggering mechanisms.

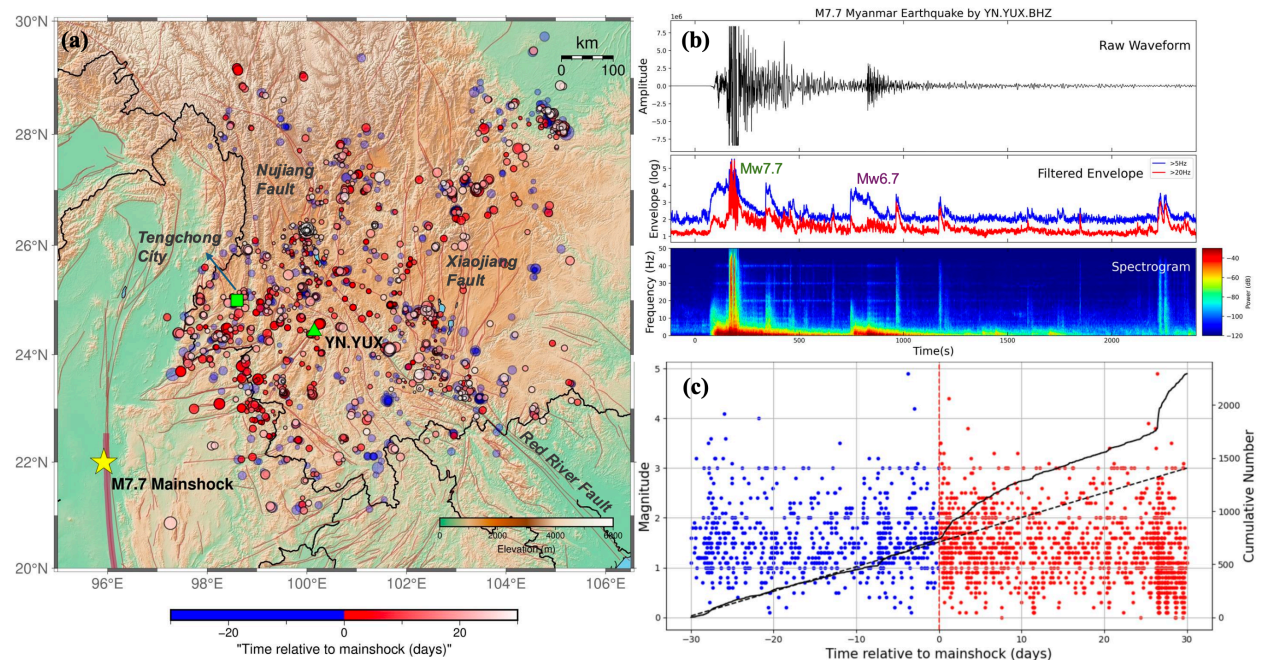


Figure 11. (a) Spatial distribution of earthquakes within 30 days before and after the 2025 Mw 7.7 Myanmar mainshock (yellow star), with event colors indicating the time relative to the mainshock (blue for before, red for after). Station locations are marked with red triangles, and sparse station names are labeled using network and station codes for clarity. (b) Seismic waveform recorded at station YN.YUX on the vertical (BHZ) component. From top to bottom: the raw waveform, log-scaled high-frequency envelopes filtered at 5 (blue) and 20 (red) Hz, and the corresponding spectrogram. The Mw 7.7 mainshock and the Mw 6.7 aftershock are highlighted in the envelope panel. (c) Time–magnitude plot of earthquakes relative to the mainshock, with blue and red dots representing events occurring before and after the mainshock,

respectively. The black curve shows the cumulative number of events during the 60-day window. The dashed line marks the expected number based on the seismicity before the mainshock.

The Xinfengjiang Reservoir in the Guangdong province in South China represents one of only four documented cases globally where reservoir has occurred $M \geq 6$ seismic events (Foulger et al., 2018). Following the 1962 $M6.1$ mainshock, persistent low-magnitude seismic activity ($ML < 3$) has been systematically recorded in this region. The physical mechanisms driving this sustained seismicity remain unresolved (Huang et al., 2025). To enhance seismic monitoring capabilities, the Guangdong Earthquake Agency has established a comprehensive broadband seismic network encompassing the reservoir area. Based on these data, our analysis reveals a notable seismicity pattern associated with the 2025 $M 7.7$ earthquake. Prior to this teleseismic event, seismic activity in the eastern reservoir (marked by the red rectangle in Figure 12) remained exceptionally low (5 detectable events) during the last 1 years. Remarkably, within one week following the mainshock, this area experienced a four-times increase in seismicity (>35 events, $ML -0.8$ to 1.3). This abrupt activation, exhibiting temporal correlation with distant seismic waves and characteristic magnitude distribution patterns, strongly suggests dynamic stress triggering mechanisms. We find no additional evidence of dynamic triggering in other region within the Guangdong province.

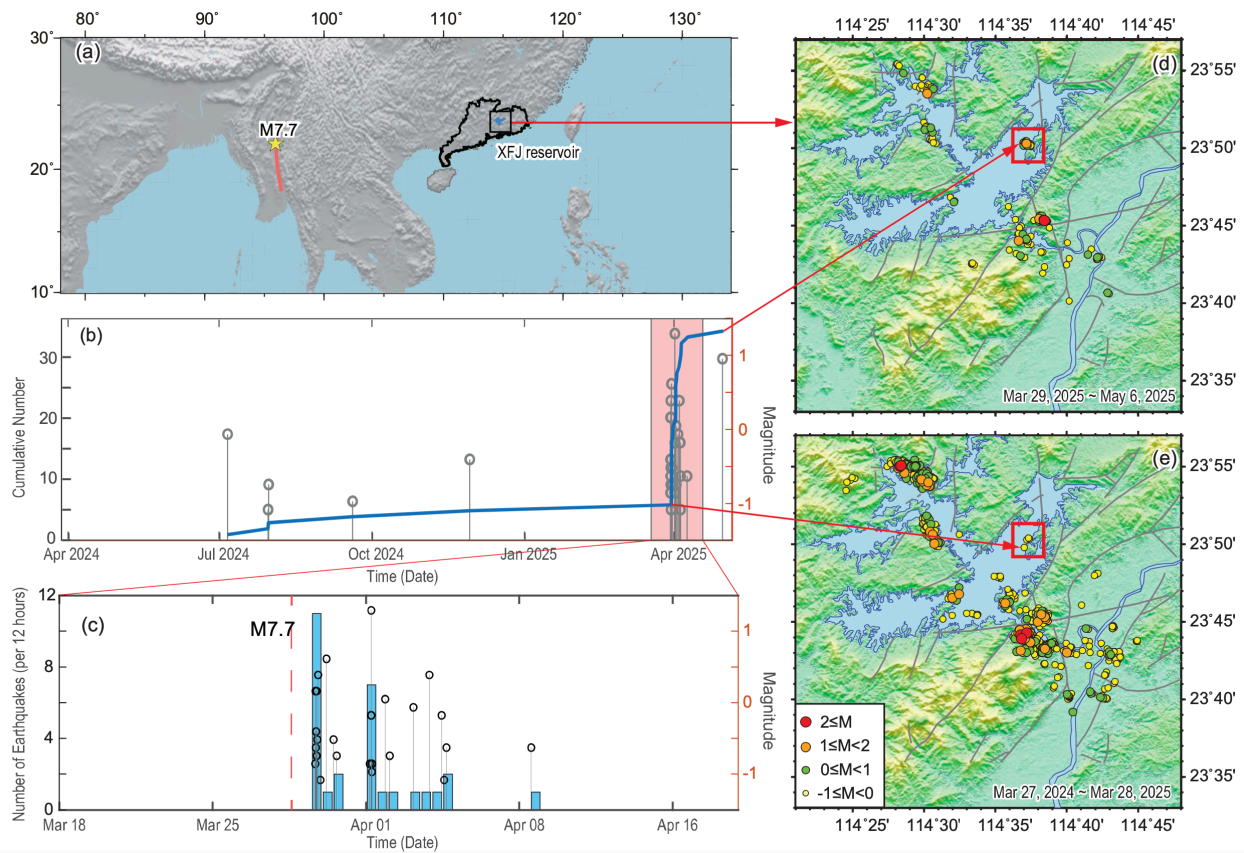


Figure 12. (a) Locations of the $M7.7$ mainshock and Xinfengjiang Reservoir. (b) Earthquake magnitude–time (M – t) plot for the region located in the southeastern wing of the Xinfengjiang Reservoir area. This region is marked by the red box in (d) and (e). (c) Cumulative number and magnitude of earthquakes shown in the shading period in (b). (d) Spatial distribution of

earthquakes one month after the M7.7 mainshock. (e) Spatial distribution of earthquakes one year before the M7.7 mainshock.

Discussions

In this study, we perform a detailed analysis of the mainshock rupture properties, initial rupture phases, tidal stress modulations of the mainshock timing, Coulomb stress changes from the mainshock and aftershocks, and remotely triggered seismicity following the M7.7 mainshock. While many of the analysis can be considered as preliminary, we can make several interesting observations. First, the mainshock rupture length of up to 500 km can be rapidly determined both from the back-projection of the teleseismic P waves, and early aftershock locations within a few hours following the mainshock (Figures 2 and 3). Subsequent analysis based on teleseismic back-projection and finite-fault inversions, as well as space geodesy observations further confirmed this ultra-long rupture (Bradley and Hubbard, 2025; Wei et al., 2025; Xu et al., 2025). However, these analyses typically took a few days/weeks to complete and hence would not be applicable immediately following the mainshock. Figure 5 also showed that many more early aftershocks were recorded by stations at regional distances, but were not detected/located yet, likely due to their overlapping arrivals. Applying advanced earthquake detection/association methods such as template matching, source scanning or machine learning can help to rapidly determine the spread of the aftershock zone (Peng and Zhao, 2009; Liao et al., 2012; Yu and Wang, 2022). Combining with teleseismic back-projection of mainshock ruptures (Wang et al., 2016a; Wei et al., 2025), these approaches can help to define the full extent of the mainshock rupture zone within hours, which are essential for rapid source characterization and subsequent aftershock forecasting.

A rupture length of ~500 km for this event (Figure 13a) would be comparable to (or even longer than) the 1906 M7.9 San Francisco earthquake, which ruptured along the San Andreas Fault in northern California for about 480 km (Song et al., 2008). However, such a long rupture length is somewhat expected for large continental strike-slip faults, which tends to have rupture length/width ratio of 20-30 (Weng and Ampuero, 2019). Recent examples include the 2001 M7.9 Kokoxili earthquake in Central Tibetan Plateau (~390 km long), and the 2002 M7.9 Denali Fault earthquake in Alaska (~340 km) (Ozacar and Beck, 2004). These events likely represent the runaway unstable ruptures (Xu et al., 2015) that can only be stopped by geometric complexities or barrier (Wesnousky, 2006).

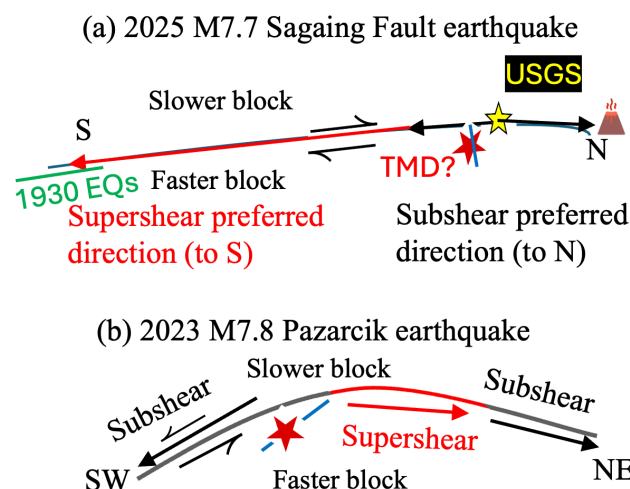


Figure 13. A comparison of a relatively simple earthquake rupture for the 2025 M7.7 Sagaing Fault earthquake in Myanmar (a), and a slightly complicated earthquake rupture for the 2023 M7.8 Pazarcik earthquake along the East Anatolian Fault in Southcentral Türkiye (b). The red lines mark the sections where the rupture went supershear for both events. The preferred direction for subshear rupture is to the slip direction of the side with lower seismic velocity, while the preferred direction for supershear is to the slip direction of the faster side (Shi and Ben-Zion, 2006). Panel (b) is modified from Peng et al. (2025).

Perhaps the most striking feature of this event is its apparent simple mainshock rupture properties (Figure 13a). Unlike the 2023 M7.8 Pazarcik event in the Kahramanmaraş Earthquake Sequence in Southeastern Türkiye (Figure 12b), which started on a subsidiary Narli fault before jumping on the main East Anatolian Fault (Xu et al., 2023; Stein and Bird, 2024), the recent M7.7 earthquake nucleated on or near the north-south striking Sagaing Fault (USGS location). However, a close-examination of the first few seconds of the near-field seismogram revealed a possible small event right before the main slip pulse (Figure 5). It is interesting to note that the TMD location of the M7.7 mainshock was about 40 km south of the USGS location, and about 20 km away from the Sagaing Fault. Because of a systematic shift of the TMD catalog to the right side (likely due to the one-side network location), we cannot verify whether the initial event was on the Sagaing Fault or not. However, it is interesting to note that the latitude of the mainshock location from the TMD catalog agreed well with the relocation from another effort (Wei et al., 2025), although their longitudes differ by 15 km. In addition, a broad aftershock zone of up to 100 km to the east of the Sagaing Fault can be seen just south of 22°N. If we cannot attribute all the distribution to the systematic shift in the TMD location (~25 km on average), then there is a significant portion of aftershocks that are off the Sagaing Fault in that region. Note that this region is in the apparent stress shadow of the mainshock (for either N-S striking or E-W striking fault) (Figures 8 and 9, and Toda and Stein (2025)). We hypothesize that the E-W distribution of aftershocks in that region could be generated by an initial E-W rupture that is conjugate to the N-S striking Sagaing Fault (Figure 13a). In this case, the initial rupture of the M7.7 mainshock would be consistent with the inference of large strike-slip earthquakes initiating from a subsidiary fault (Stein and Bird, 2025). Such interpretation is also similar to the M4.7 foreshock occurring on a conjugated fault before the 2010 M6.7 Yushu earthquake within the Tibetan plateau (Chuang et al., 2023). The only difference is that the time separation between the foreshock and the mainshock for the Yushu sequence is about 2 hours, while in this case, there is virtually no time delay. Hence, it can be recognized as an immediate foreshock, such as the M5.9 foreshock ~14 s before the 2024 M7.6 Noto Peninsula earthquake in western Japan (Peng et al., 2025), or the ‘nucleation’/beginning of the mainshock rupture (e.g., the initial rupture of the 2023 M7.8 Pazarcik earthquake) (Peng et al., 2025; Peng and Lei, 2025). A systematic relocation effort for both the initial rupture location and the main slip pulses that includes all regional stations available (likely stations from Southwest China and Eastern India) is needed to confirm or reject the hypothesis that the initial mainshock rupture occurred away from the Sagaing Fault (Figure 13a).

Despite possible complications in the initial mainshock rupture, the main ruptured fault segment is very simple without obvious fault kinks or step overs (Wei et al., 2025; Li et al., 2025). The mainshock first ruptured towards north along the Sagaing Fault for about 100 km with a subshear velocity (Figure 2). The southward rupture also started with a subshear velocity for about 100 km, and then the rupture went supershear for another 300 km (Figure 2) (Wei et al., 2025). However, Li et al. (2025) argued that the supershear ruptures started immediately south of the mainshock epicenter. The northward rupture ended near the Singu Plateau, which likely acted as a barrier for the 2012 Mw 6.8 Thabeikkyin earthquake and the 2025 M7.7 ruptures (Wei et al., 2025). The southern end of the 2025 rupture zone partially overlaps with the rupture zone of several M6-7 earthquakes in 1929-1930 (Wang et al., 2014; Wei et al., 2025). In summary, the 2025 M7.7 mainshock rupture likely represent one end-member model of large continental strike-slip fault with very simple geometry (Figure 13a) and no obvious branching or subsidiary fault ruptures. Other examples include the 1906 M7.9 San Francisco earthquake (Song

et al., 2008). The other end-member model would be the complex fault rupture such as the 2023 M7.8 Pazarcik earthquakes (Figure 13b) and events documented in Stein and Bird (2024).

As noted before, aftershocks from the regional TMD catalog were mostly shifted to the right side of the Sagaing Fault in the Shan Plateau (Figure 4). However, large aftershocks from the USGS catalog were mostly on or very close to the Sagaing Fault (Figure 4d). At least part of the shift can be explained by the one-side station distribution of the TMD catalog. However, the average shift (by assuming that the USGS location is accurate) is about 25 km (Figure 4f), which cannot completely explain all aftershocks with some of them extending more than 75 km to the east of the Sagaing Fault. A simple explanation of those off-fault aftershocks can be reactivation of subsidiary faults within or near the Shan Plateau such as the Shan Scarp Fault (Bertrand et al., 1999), which are oriented at a certain angle to the Sagaing Fault. Such an off-fault aftershock activation would be more prominent especially during the supershear rupture segments of previous large strike-slip earthquakes (Bouchon and Karabulut, 2008). An alternative explanation would be that the Sagaing Fault is dipping to the east, which is consistent with inversions of GNSS observations (Tin et al., 2022). However, some finite-fault inversions argued a near-vertical rupture (USGS, 2025; Wei et al., 2025). Again, a careful detection and relocation of aftershocks following the M7.7 mainshock is needed to better understand the relationship between subshear/supershear mainshock ruptures and on-fault/off-fault aftershocks.

Recent permanent and temporary seismic deployments across and along the Sagaing Fault have resulted in high-resolution imaging of subsurface crustal structures on both sides of the faults. These studies found that in the top few kms of the crust, the Central Myanmar Basin (CMB) in the Burma plate on the left side of the Sagaing Fault has slower seismic velocities than the Shan Plateau in the Sunda plate on the right side (Wang et al., 2019; Wu et al., 2021; Yao et al., 2022). Our initial observation of possible fault zone head waves at station GE.NPW (Figure 7) also confirmed that the CWB side has slower velocity than the Shan Plateau. The existence of such a bi-material fault interface is expected to affect many aspects of earthquake source properties, including generation of a preferred rupture direction in the slip direction of the slower/more compliant block for a sub-shear rupture (e.g., Ben-Zion, 2001; Ampuero and Ben-Zion, 2008). For a supershear rupture, the propagation direction is flipped (i.e., in the slip direction of the faster/stiffer side) (Weertman, 2002; Shi and Ben-Zion, 2006). In addition to the “preferred” rupture direction, dynamic ruptures on bi-material interface can generate asymmetric fault damage zone at depth (Shi and Ben-Zion, 2006). For a sub-shear rupture, the ‘preferred’ off-fault damage is on the stiffer side (Jara et al., 2021; Song et al., 2022), while the pattern is flipped again for the supershear rupture (i.e., on the more compliant side). We note that the northward rupture along the Sagaing Fault is subshear, matching the preferred slip direction of the slow CMB block, while the southward supershear rupture also matched the preferred slip direction of the fast Shan Plateau block (Figure 13a). However, there existed a ~100 km southward subshear rupture that did not match this expectation. Additional seismic imaging studies at a finer scale (combined with fault zone waves as observed in Figure 7) can help to resolve whether the velocity contrast could be flipped in this section (e.g., Bennington et al., 2013). In addition, high-resolution optical imagery from Sentinel-2 displacement fields has been used to infer the co-seismic damage zones of ~100 m width following the M7.7 mainshock (Wei et al., 2025). However, no asymmetric fault damage zone has been inferred, likely due to the lack of accurate surface rupture traces. Additional field surveys, together with dense cross-fault

seismic arrays (Zor et al., 2025), can be used to further constrain the low-velocity damage zones at depth, and their relationship with dynamic earthquake ruptures.

We document clear evidence of remotely triggered seismicity near the border between Thailand and Myanmar, nearby Yunnan province in China, and the Xinfengjiang Reservoir in the Guangdong province in South China (Figures 10-12). In most cases, seismicity started during and immediately following the large-amplitude surface waves, although in most cases large local events typically occurred a few hours to days following the mainshock, likely representing delayed dynamic triggering (Pollitz et al., 2012; Johnson and Bürgmann, 2016). In addition, many regions are a few fault lengths away from the M7.7 mainshock, where static stress changes became much lower than the dynamic stress changes. However, some regions, such as the border between Thailand and Myanmar are relatively close to the M7.7 mainshock rupture and hence could be affected by the static stress changes. While we do not have the focal mechanisms of most triggered earthquakes, focal mechanisms of moderate-size events in this region are mostly N-S or E-W strike slip, which would receive negative CFS (i.e., stress shadow) from the M7.7 mainshock slip (Figure 8). This observation is consistent with other recent observations where microearthquakes in the static stress shadow of a mainshock can be instantaneously or delayed triggered by the dynamic stresses of the same mainshock rupture (Ma et al., 2005; Meng and Peng, 2014; Hardebeck and Harris, 2022; Yun et al., 2025). It would be interesting to observe whether in the long-term (i.e., after a few months when the effect of the dynamic stress is over), seismicity in the surrounding region would match with the prediction from the static stress changes from the M7.7 mainshock (Li et al., 2025; Toda and Stein, 2025).

Finally, we note that this section that ruptured during the M7.7 mainshock has long been recognized as a region that is long due for a major earthquake (Wang et al., 2014; Xiong et al., 2017; Habbard and Bradley, 2025). Although the location and its magnitude (to a less degree) can be anticipated, at this point we cannot accurately predict the timing of such a major earthquake. In addition, while the mainshock timing might be promoted by the tidal stresses (Figure 8), there was no obvious foreshocks or other abnormal behaviors (at least seismically). The lack of reliable precursory signals highlights the challenge that earthquake scientists has been facing in the last half a century since the prediction of the 1975 Ms7.3 Haicheng earthquake (Wang et al., 2006; Peng and Lei, 2025). Nevertheless, multiple groups have deployed both permanent seismic network and temporary seismic arrays across and along the Sagaing Fault in the past decade (Thiam et al., 2017; Wang et al., 2019; Wu et al., 2021; Yao et al., 2022). Unfortunately, none of those temporary seismic arrays were active in 2025, and only 4 of the 9 stations in the Myanmar National Seismic Network (netcode: MM) were in operation during the mainshock. Station GE.NPW operated by GFZ provided a clear single near-field recording of the mainshock ruptures (Lai et al., 2025; Figure 6). Better understanding of the large earthquakes requires long-term deployment and investments of near-fault zone arrays (Ben-Zion et al., 2022), possibly including motion-sensor cameras and video recordings (Latour et al., 2025) and earthquake experiment sites (Wu, 2022) at regions where large earthquakes are due. These include regions such as the North-South Seismic Belt in China (Wu, 2022), the Southern Section of the San Andreas Fault (Fialko, 2006) and the Marmara Sea section of the North Anatolian Fault (NAF) near Istanbul (Becker et al., 2023).

Acknowledgements We thank the Thai Meteorological Department (TMD) for making their earthquake catalog available for this study. Most seismic data are downloaded from the Earthscope Inc. (formally known as IRIS)'s Data Management Center at the following website:

https://ds.iris.edu/wilber3/find_stations/11952284. Waveform data from NPW can be retrieved from GEOFON using the FDSN. The velocity seismogram at station NPW is downloaded from <https://doi.org/10.5281/zenodo.15228691> (Bindi et al., 2025). Earthquake catalogs in China are provided by the Yunnan and Guangdong Earthquake Agency. We thank valuable comments and discussions with Professors Shengji Wei and Jing Wu.

References

Ampuero, J. P., & Ben-Zion, Y. (2008). Cracks, pulses and macroscopic asymmetry of dynamic rupture on a bimaterial interface with velocity-weakening friction. *Geophysical Journal International*, 173(2), 674-692. <https://doi.org/10.1111/j.1365-246X.2008.03736.x>

Becker, D., Martínez-Garzón, P., Wollin, C., Kılıç, T., & Bohnhoff, M. (2023), Variation of fault creep along the overdue Istanbul-Marmara seismic gap in NW Türkiye. *Geophysical Research Letters*, 50, <https://doi.org/10.1029/2022GL101471>

Bennington, N. L., C. Thurber, Z. Peng, H. Zhang, & P. Zhao (2013), Incorporating fault zone head wave and direct wave secondary arrival times into seismic tomography: Application at Parkfield, California, *J. Geophys. Res.*, 118, 1-7, doi: 10.1002/jgrb.50072.

Ben-Zion, Y. (2001). Dynamic ruptures in recent models of earthquake faults. *Journal of the Mechanics and Physics of Solids*, 49(9), 2209-2244. [https://doi.org/10.1016/S0022-5096\(01\)00036-9](https://doi.org/10.1016/S0022-5096(01)00036-9)

Ben-Zion, Y., & Malin, P. (1991). San Andreas fault zone head waves near Parkfield, California. *Science*, 251(5001), 1592-1594. <https://doi.org/10.1126/science.251.5001.1592>

Ben-Zion, Y., Beroza, G. C., Bohnhoff, M., Gabriel, A. A., & Mai, P. M. (2022). A grand challenge international infrastructure for earthquake science. *Seismological Society of America*, 93(6), 2967-2968.

Bertrand, G., & Rangin, C. (2003). Tectonics of the western margin of the Shan plateau (central Myanmar): implication for the India–Indochina oblique convergence since the Oligocene. *Journal of Asian Earth Sciences*, 21(10), 1139-1157. [https://doi.org/10.1016/S1367-9120\(02\)00183-9](https://doi.org/10.1016/S1367-9120(02)00183-9)

Bertrand, G., Rangin, C., Maluski, H., Han, T.A., Thein, M., Myint, O., Maw, W. & Lwin, S. (1999). Cenozoic metamorphism along the Shan scarp (Myanmar): evidences for ductile shear along the Sagaing fault or the northward migration of the eastern Himalayan syntaxis?. *Geophysical Research Letters*, 26(7), 915-918. <https://doi.org/10.1029/1999GL900136>

Bindi, D., Lai, S.-T., Strollo, A., Zaccarelli, R., & Tilmann, F. (2025). Software and data products for "Capacity Building Enables Unique Near-Fault Observations of the destructive 2025 Mw 7.7 Myanmar Earthquake", Zenodo, <https://doi.org/10.5281/zenodo.15228691>.

Bouchon, M., & Karabulut, H. (2008). The aftershock signature of supershear earthquakes. *Science*, 320(5881), 1323-1325. <https://doi.org/10.1126/science.1155030>.

690 Bouchon, M., Bouin, M. P., Karabulut, H., Toksöz, M. N., Dietrich, M., & Rosakis, A. J. (2001).
691 How fast is rupture during an earthquake? New insights from the 1999 Turkey earthquakes.
692 Geophysical Research Letters, 28(14), 2723-2726. <https://doi.org/10.1029/2001GL013112>

693 Bouchon, M., Karabulut, H., Aktar, M., Özalaybey, S., Schmittbuhl, J., & Bouin, M. P. (2011).
694 Extended nucleation of the 1999 Mw 7.6 Izmit earthquake. *science*, 331(6019), 877-880.
695 <https://doi.org/10.1126/science.1197341>

696 Bradley, K., & Hubbard, J. (2024). The great tidal earthquake hypothesis test, part III.
697 Earthquake Insights, <https://doi.org/10.62481/3b93879a>

698 Bradley, K., & Hubbard, J. (2025a). Updates on the M7.7 Myanmar earthquake. Earthquake
699 Insights, <https://doi.org/10.62481/9e49eb4a>

700 Bradley, K., & Hubbard, J. (2025b). Surface ruptures of the Myanmar M7.7 earthquake mapped
701 from space. Earthquake Insights, <https://doi.org/10.62481/51b7df8c>

702 Cai, J., Xi, N., Han, G., Deng, W., & Sun, L. (2025). Rapid report of the March 28, 2025 Mw 7.9
703 Myanmar earthquake. *Earthquake Research Advances*, 100396.
704 <https://doi.org/10.1016/j.eqrea.2025.100396>

705 Chansom, C., Jitmahantakul, S., Owen, L. A., Wiwegwin, W., & Charusiri, P. (2022). New
706 insights into the paleoseismic history of the Mae Hong Son Fault, northern Thailand. *Frontiers in*
707 *Earth Science*, 10, 921049. <https://doi.org/10.3389/feart.2022.921049>

708 Crosetto, S., Watkinson, I. M., Min, S., Falcucci, E., Gori, S., Thein, P. S., & Sudeep. (2019).
709 Searching for the 1912 Maymyo earthquake: New evidence from paleoseismic investigations
710 along the Kyaukkyan Fault, Myanmar. *Quaternary International*, 532, 75–86.
711 <https://doi.org/10.1016/j.quaint.2019.09.042>

712 Chuang, L. Y., Peng, Z., Lei, X., Wang, B., Liu, J., Zhai, Q., & Tu, H. (2023), Foreshocks of the
713 2010 Mw 6.7 Yushu, China Earthquake Occurred Near an Extensional Step-Over, *J. Geophys.*
714 *Res.*, 128, e2022JB025176. <https://doi.org/10.1029/2022JB025176>.

715 Dziewonski, A., Hales, A., & Lapwood, E. (1975). Parametrically simple Earth models
716 consistent with geophysical data. *Phys. Earth Planet. Inter.* 10(1), 12–48.
717 [https://doi.org/10.1016/0031-9201\(75\)90017-5](https://doi.org/10.1016/0031-9201(75)90017-5)

718 Ellsworth, W. L., & Beroza, G. C. (1995). Seismic evidence for an earthquake nucleation phase.
719 *Science*, 268(5212), 851-855. <https://doi.org/10.1126/science.268.5212.851>

720 Fialko, Y. (2006). Interseismic strain accumulation and the earthquake potential on the southern
721 San Andreas fault system. *Nature*, 441(7096), 968-971. <https://doi.org/10.1038/nature04797>

722 Foulger, G. R., Wilson, M. P., Gluyas, J. G., Julian, B. R., & Davies, R. J. (2018). Global review
723 of human-induced earthquakes. *Earth-Science Reviews*, 178, 438-514.
724 <https://doi.org/10.1016/j.earscirev.2017.07.008>

725 Gahalaut, V. K., & Gahalaut, K. (2007), Burma plate motion, *J. Geophys. Res.*, 112, B10402,
726 <https://doi.org/10.1029/2007JB004928>.

727 Hardebeck, J.L., & Harris, R.A. (2022). Earthquakes in the Shadows: Why Aftershocks Occur at
728 Surprising Locations. *The Seismic Record*, 2(3), 207–216. <https://doi.org/10.1785/0320220023>

729 Henry, C., & Das, S. (2001). Aftershock zones of large shallow earthquakes: fault dimensions,
730 aftershock area expansion and scaling relations. *Geophysical Journal International*, 147(2), 272-
731 293. <https://doi.org/10.1046/j.1365-246X.2001.00522.x>

732 Hough, S. E. (2018). Do large (magnitude ≥ 8) global earthquakes occur on preferred days of the
733 calendar year or lunar cycle?. *Seismological Research Letters*, 89(2A), 577-581.
734 <https://doi.org/10.1785/0220170154>.

735 Hu, X.P., Zang, A., Heidbach, O., Cui, X.F., Xie, F.R., & Chen, J.W. (2017). Crustal stress
736 pattern in China and its adjacent areas. *J. Asian Earth Sci.* 149, 20-28,
737 <https://doi.org/10.1016/j.jseaes.2017.07.005>.

738 Huang, R.Q., Deng, Y.F, Chen, Y., Xiong, C., & Zhang, Z. (2025). Source parameters and stress
739 triggering of 2023 $M \geq 4$ earthquakes sequence in Heyuan, Guangdong. *Chinese Journal of*
740 *Geophysics (in Chinese with English abstract)*, 68(3), 956-969,
741 <https://doi.org/10.6038/cjg2024R0701>

742 Hubbard, J. & Bradley, K. (2025). Catastrophic M7.7 earthquake caused by rupture of Sagaing
743 Fault in Myanmar. *Earthquake Insights*, <https://doi.org/10.62481/9250a38a>

744 Ide, S., Yabe, S., & Tanaka, Y. (2016). Earthquake potential revealed by tidal influence on
745 earthquake size–frequency statistics. *Nature Geoscience*, 9(11), 834-837.
746 <https://doi.org/10.1038/ngeo2796>

747 Inoue, N., Yamaguchi, R., Yagi, Y., Okuwaki, R., Bogdan, E., & Tadapansawut, T. (2025). A
748 multiple asymmetric bilateral rupture sequence derived from the peculiar tele-seismic P-waves of
749 the 2025 Mandalay, Myanmar earthquake. *Seismica*, 4(1).
750 <https://doi.org/10.26443/seismica.v4i1.1691>

751 Iwata, T. (2008). Low detection capability of global earthquakes after the occurrence of large
752 earthquakes: Investigation of the Harvard CMT catalogue. *Geophysical Journal International*,
753 174(3), 849-856. <https://doi.org/10.1111/j.1365-246X.2008.03864.x>

754 Jackson, D.D., & Kagan, Y.Y. (2011). Characteristic Earthquakes and Seismic Gaps. In: Gupta,
755 H.K. (eds) *Encyclopedia of Solid Earth Geophysics*. *Encyclopedia of Earth Sciences Series*.
756 Springer, Dordrecht. https://doi.org/10.1007/978-90-481-8702-7_181

757 Jara, J., Bruhat, L., Thomas, M. Y., Antoine, S. L., Okubo, K., Rougier, E., Rosakis, A. J., Sammis,
758 C. G., Klinger, Y., Jolivet, R., & Bhat, H. S. (2021). Signature of transition to supershear rupture
759 speed in the coseismic off-fault damage zone. *Proceedings of the Royal Society A*, 477(2255),
760 20210364. <https://doi.org/10.1098/rspa.2021.0364>

761 Johnson, C. W., and R. Bürgmann (2016), Delayed dynamic triggering: Local seismicity leading
762 up to three remote $M \geq 6$ aftershocks of the 11 April 2012 M8.6 Indian Ocean earthquake, J.
763 *Geophys. Res. Solid Earth*, 121, 134–151, doi:10.1002/2015JB012243.

764 Kagan, Y. Y. (2004). Short-term properties of earthquake catalogs and models of earthquake
765 source. *Bulletin of the Seismological Society of America*, 94(4), 1207-1228.
766 <https://doi.org/10.1785/012003098>

767 Kagan, Y., Jackson, D. D., & Geller, R. J. (2012). Characteristic earthquake model, 1884--2011,
768 RIP. arXiv preprint <https://arxiv.org/pdf/1207.4836>

769 Kiser, E., & Ishii, M. (2017). Back-projection imaging of earthquakes. *Annual Review of Earth*
770 *and Planetary Sciences*, 45(1), 271-299. <https://doi.org/10.1146/annurev-earth-063016-015801>

771 Kwiatek, G., Martínez-Garzón, P., Becker, D., Dresen, G., Cotton, F., Beroza, G.C., Acaarel, D.,
772 Ergintav, S. & Bohnhoff, M. (2023). Months-long seismicity transients preceding the 2023 MW
773 7.8 Kahramanmaraş earthquake, Türkiye. *Nature Communications*, 14(1), 7534.
774 <https://doi.org/10.1038/s41467-023-42419-8>

775 Lai, S.T., Oo, K.M., Htwe, Y.M.M., Yi, T., Than, H.H., Than, O., Min, Z., Oo, T.M., Maung,
776 P.M., Bindi, D. & Cotton, F. (2025). Capacity Building Enables Unique Near-Fault Observations
777 of the destructive 2025 M w 7.7 Myanmar Earthquake. *Earth System Science Data Discussions*,
778 2025, in review. <https://doi.org/10.5194/essd-2025-216>

779 Latour, S., Lebihain, M., Bhat, H. S., Twardzik, C., Bletery, Q., Hudnut, K. W., & Passelègue, F.
780 (2025). Direct Estimation of Earthquake Source Properties from a Single CCTV Camera.
781 <https://arxiv.org/abs/2505.15461>.

782 Lei, X., C. Xie, and B. Fu (2011), Remotely triggered seismicity in Yunnan, southwestern China,
783 following the 2004 Mw9.3 Sumatra earthquake, *J. Geophys. Res.*, 116, B08303,
784 doi:10.1029/2011JB008245.

785 Lengine, O., B. Enescu, Z. Peng, and K. Shiomi (2012), Decay and migration of the early
786 aftershock activity following the Tohoku Mw9.0 2011 earthquake, *Geophys. Res. Lett.*, 39,
787 L18309, doi:10.1029/2012GL052797.

788 Li, L., Wang, B., Peng, Z., & Li, D. (2019). Dynamic triggering of microseismicity in Southwest
789 China following the 2004 Sumatra and 2012 Indian Ocean earthquakes. *Journal of Asian Earth*
790 *Sciences*, 176, 129-140. <https://doi.org/10.1016/j.jseaes.2019.02.010>

791 Li, T., & Song, X. (2025). Moment Magnitude of Myanmar Earthquake on March 28, 2025 from
792 Long-Period Seismic Coda, *Earthquake Sciences*, in review.
793 <https://dx.doi.org/10.2139/ssrn.5220290>

794 Li, Y., Yang, C., Hu, X., Yuan, J., Yao, G. & Li, H. (2025). Coulomb Stress Transfer from the
795 2025 Mw 7.7 Myanmar Earthquake to Active Faults in Southwestern Yunnan, China:
796 Implications for Seismic Hazard. *Earthquake Research Advances*, revised.

797 Liao, Y.C., Kao, H., Rosenberger, A., Hsu, S.K. & Huang, B.S. (2012). Delineating complex
798 spatiotemporal distribution of earthquake aftershocks: an improved Source-Scanning
799 Algorithm, *Geophysical Journal International*, 189(3), 1753-
800 1770, <https://doi.org/10.1111/j.1365-246X.2012.05457.x>

801 Lindsey, E.O., Wang, Y., Aung, L.T., Chong, J.H., Qiu, Q., Mallick, R., Feng, L., Aung, P.S.,
802 Tin, T.Z.H., Min, S.M. & Bradley, K. (2023). Active subduction and strain partitioning in

western Myanmar revealed by a dense survey GNSS network. *Earth and Planetary Science Letters*, 622, 118384, <https://doi.org/10.1016/j.epsl.2023.118384>.

Ma, K.-F., Chan, C.-H., & Stein, R. S. (2005). Response of seismicity to Coulomb stress triggers and shadows of the 1999 Mw = 7.6 Chi-Chi, Taiwan, earthquake, *J. Geophys. Res.*, 110, B05S19, doi:10.1029/2004JB003389.

Ma, Z., Zeng, H., Luo, H., Liu, Z., Jiang, Y., Aoki, Y., Wang, W., Itoh, Y., Lyu, M., Cui, Y., Yun, S.H., Hill, E.M., & Wei, S. (2024). Slow rupture in a fluid-rich fault zone initiated the 2024 Mw 7.5 Noto earthquake. *Science*, 385(6711), 866-871. <https://doi.org/10.1126/science.ado5143>

Mallick, R., Lindsey, E. O., Feng, L., Hubbard, J., Banerjee, P., & Hill, E. M. (2019). Active convergence of the India- Burma-Sunda plates revealed by a new continuous GPS network. *Journal of Geophysical Research: Solid Earth*, 124, 3155–3171. <https://doi.org/10.1029/2018JB016480>.

Matsumoto, K., Sato, T., Takanezawa, T., & Ooe, M. (2001). GOTIC2: a program for computation of oceanic tidal loading effect. *J. Geod. Soc. Jpn.* 47, 243–248. <https://doi.org/10.11366/sokuchi1954.47.243>

McCaffrey, R. (2009). The tectonic framework of the Sumatran subduction zone. *Annual Review of Earth and Planetary Sciences*, 37(1), 345-366. <https://doi.org/10.1146/annurev.earth.031208.100212>

Meng, X. and Z. Peng (2014), Seismicity rate changes in the San Jacinto Fault Zone and the Salton Sea Geothermal Field following the 2010 Mw7.2 El Mayor-Cucapah Earthquake, *Geophys. J. Int.*, 197(3), 1750-1762, doi: 10.1093/gji/ggu085.

Mogi, K. (1979). Two kinds of seismic gaps. *Pure and Applied Geophysics*, 117(6), 1172-1186. <https://doi.org/10.1007/BF00876213>

Nielsen, C., Chamot-Rooke, N., Rangin, C., The ANDAMAN Cruise Team, 2004. From partial to full strain partitioning along the Indo-Burmese hyper-oblique subduction. *Marine Geology* 209, 303–327. <https://doi.org/10.1016/j.margeo.2004.05.001>

Ozacar, A.A., & Beck, S.L. (2004). The 2002 Denali fault and 2001 Kunlun fault earthquakes: complex rupture processes of two large strike-slip events. *Bull. Seismol. Soc. Am.* 94 (6B), S278–S292. <https://doi.org/10.1785/0120040604>.

Peng, Z., & Chao, K. (2008). Non-volcanic tremor beneath the Central Range in Taiwan triggered by the 2001 Mw7.8 Kunlun earthquake, *Geophys. J. Int.*, 175, 825–829, doi: 10.1111/j.1365-246X.2008.03886.x.

Peng, Z., & Zhao, P. (2009). Migration of early aftershocks following the 2004 Parkfield earthquake. *Nature Geosci* 2, 877–88. <https://doi.org/10.1038/ngeo697>

Peng, Z. & Gomberg, J. (2010), An integrated perspective of the continuum between earthquakes and slow-slip phenomena, *Nature Geosci.*, 3, 599–607, doi:10.1038/ngeo940.

Peng, Z., and X. Lei (2025), Physical Mechanisms of Earthquake Nucleation and Foreshock: Cascade Triggering, Aseismic Slip, or Fluid Flows?, *Earthquake Research Advances*, 5(2), 100349, <https://doi.org/10.1016/j.eqrea.2024.100349>.

842 Peng, Z., Vidale, J.E. & Houston, H. (2006). Anomalous early aftershock decay rates of the 2004
843 M6 Parkfield earthquake, *Geophys. Res. Lett.*, 33, L17307, doi:10.1029/2006GL026744.

844 Peng, Z., X. Lei, Q.-Y. Wang, D. Wang, P. Mach, D. Yao, A. Kato, K. Obara and M. Campillo
845 (2025), The Evolution Process between the Earthquake Swarm Beneath the Noto Peninsula,
846 Central Japan and the 2024 M 7.6 Noto Hanto Earthquake Sequence, *Earthquake Research*
847 *Advances*, 5(1), 100332, <https://doi.org/10.1016/j.eqrea.2024.100332>.

848 Prejean, S. G., Hill, D. P., Brodsky, E. E., Hough, S. E., Johnston, M. J. S., Malone, S. D., et al.
849 (2004). Remotely triggered seismicity on the United States west Coast following the Mw 7.9
850 Denali Fault earthquake. *Bulletin of the Seismological Society of America*, 94(6B), S348–S359.
851 <https://doi.org/10.1785/0120040610>

852 Pollitz, F. F., Stein, R. S., Sevilgen, V., & Bürgmann, R. (2012). The 11 April 2012 east Indian
853 Ocean earthquake triggered large aftershocks worldwide. *Nature*, 490(7419), 250–253.
854 <https://doi.org/10.1038/nature11504>

855 Ren, C., Wang, Z., Taymaz, T., Hu, N., Luo, H., Zhao, Z., Yue, H., Song, X., Shen, Z., Xu, H.
856 and Geng, J., 2024. Supershear triggering and cascading fault ruptures of the 2023
857 Kahramanmaraş, Türkiye, earthquake doublet. *Science*, 383(6680), 305–311.
858 <https://doi.org/10.1126/science.adf1519>

859 Robinson, D. P., Das, S., & Searle, M. P. (2010). Earthquake fault superhighways.
860 *Tectonophysics*, 493(3–4), 236–243. <https://doi.org/10.1016/j.tecto.2010.01.010>

861 Ruan, Y. (2007). Source parameters and triggering mechanism of the Nansang earthquake
862 triggered by the Sumatra earthquake. M.S. Thesis, University of Science and Technology of
863 China, 59 pages.

864 Song, B. R., Song, W. J., Johnson, S. E., Gerbi, C. C., & Vel, S. S. (2022). Elastic contrast, rupture
865 directivity, and damage asymmetry in an anisotropic bimaterial strike-slip fault at middle crustal
866 depths. *Journal of Geophysical Research: Solid Earth*, 127, e2021JB023821.
867 <https://doi.org/10.1029/2021JB023821>

868 Song, S. G., Beroza, G. C., & Segall, P. (2008). A unified source model for the 1906 San
869 Francisco earthquake. *Bulletin of the Seismological Society of America*, 98(2), 823–831,
870 <https://doi.org/10.1785/0120060402>

871 Shahzada, K., Noor, U. A., & Xu, Z.D. (2025). In the Wake of the March 28, 2025 Myanmar
872 Earthquake: A Detailed Examination, *Journal of Dynamic Disasters*,
873 <https://doi.org/10.1016/j.jdd.2025.100017>

874 Shi, Z., & Ben-Zion, Y. (2006). Dynamic rupture on a bimaterial interface governed by slip-
875 weakening friction. *Geophysical Journal International*, 165(2), 469–484.
876 <https://doi.org/10.1111/j.1365-246X.2006.02853.x>

877 Stein, R. (1999). The role of stress transfer in earthquake occurrence. *Nature* 402, 605–609.
878 <https://doi.org/10.1038/45144>

879 Stein, R. S., & Bird, P. (2024). Why do great continental transform earthquakes nucleate on
880 branch faults?. *Seismological Research Letters*, 95(6), 3406-3415.
881 <https://doi.org/10.1785/0220240175>

882 Tanaka, S. (2012). Tidal triggering of earthquakes prior to the 2011 Tohoku-Oki earthquake
883 (Mw 9.1). *Geophys. Res. Lett.* 39, 00G26. <https://doi.org/10.1029/2012GL051179>.

884 Thiam, H.N., Htwe, Y.M.M., Kyaw, T.L., Tun, P.P., Min, Z., Htwe, S.H., Aung, T.M., Lin,
885 K.K., Aung, M.M., Cristofaro, J.D. & Franke, M. (2017). A report on upgraded seismic
886 monitoring stations in Myanmar: Station performance and site response. *Seismological Research*
887 *Letters*, 88(3), pp.926-934.

888 Timsina, P., Hearn, T. M., & Ni, J. F. (2024). Crust and mantle flow from central Tibetan Plateau
889 to the Indo-Burma subduction zone. *Journal of Geophysical Research: Solid Earth*, 129,
890 e2023JB027540. <https://doi.org/10.1029/2023JB027540>

891 Tin, T. Z. H., Nishimura, T., Hashimoto, M., Lindsey, E. O., Aung, L. T., Min, S. M., & Thant,
892 M. (2022). Present-day crustal deformation and slip rate along the southern Sagaing fault in
893 Myanmar by GNSS observation. *Journal of Asian Earth Sciences*, 228, 105125.
894 <https://doi.org/10.1016/j.jseaes.2022.105125>

895 Toda, S. & Stein, R. S. (2025). One-month earthquake forecast for western Myanmar following
896 the devastating magnitude 7.7 Mandalay shock, Temblor, <http://doi.org/10.32858/temblor.360>

897 Tun, S.T., & Watkinson, I.M. (2017). "Chapter 19: The Sagaing Fault, Myanmar", in "Myanmar:
898 Geology, Resources and Tectonics", edited by Barber, A.J., Zaw, K. & Crow, M.J., Geological
899 Society, London, Memoirs, <https://doi.org/10.1144/m48.19>

900 USGS (2025). <https://earthquake.usgs.gov/earthquakes/eventpage/us7000pn9s/executive>

901 Utsu, T., Ogata, Y., & Matsu'ura, R.S. (1995). The centenary of the Omori formula for a decay
902 law of aftershock activity. *Journal of Physics of the Earth*, 43(1), 1-33.
903 <https://doi.org/10.4294/jpe1952.43.1>

904 Wald, D. J., Worden, C. B., Thompson, E. M., & Hearne, M. (2022). ShakeMap operations,
905 policies, and procedures. *Earthquake Spectra*, 38(1), 756-777.
906 <https://doi.org/10.1177/87552930211030298>

907 Wang, D., & Mori, J. (2011). Rupture process of the 2011 off the Pacific coast of Tohoku
908 Earthquake (M w 9.0) as imaged with back-projection of teleseismic P-waves. *Earth, planets and*
909 *space*, 63, 603-607.

910 Wang, D., Kawakatsu, H., Mori, J., Ali, B., Ren, Z., & Shen, X. (2016a). Backprojection
911 analyses from four regional arrays for rupture over a curved dipping fault: The Mw 7.7 24
912 September 2013 Pakistan earthquake. *Journal of Geophysical Research: Solid Earth*, 121(3),
913 1948-1961.

914 Wang, D., Mori, J., & Koketsu, K. (2016b). Fast rupture propagation for large strike-slip
915 earthquakes. *Earth and Planetary Science Letters*, 440, 115-126.

916 Wang, Y., K. Sieh, S. T. Tun, K.-Y. Lai, and T. Myint (2014), Active tectonics and earthquake
917 potential of the Myanmar region, *J. Geophys. Res. Solid Earth*, 119, 3767–3822,
918 doi:10.1002/2013JB010762.

919 Wang, X., Wei, S., Wang, Y., Maung Maung, P., Hubbard, J., Banerjee, P., et al. (2019). A 3-D
 920 shear wave velocity model for Myanmar region. *Journal of Geophysical Research: Solid Earth*,
 921 124, 504–526. <https://doi.org/10.1029/2018JB016622>

922 Weertman, J. (2002). Subsonic type earthquake dislocation moving at approximately \times shear
 923 wave velocity on interface between half spaces of slightly different elastic constants.
 924 *Geophysical Research Letters*, 29(10). <https://doi.org/10.1029/2001GL013916>.

925 Wei, S., Wang, X., Li, C., et al. (2025). Supershear Rupture Sustained Through a Thick Fault
 926 Zone in the 2025 Mw 7.8 Myanmar Earthquake, submitted.

927 Wells, D.L. & Coppersmith, K.J. (1994). New empirical relationships among magnitude, rupture
 928 length, rupture width, rupture area, and surface displacement. *Bulletin of the seismological*
 929 *Society of America*, 84(4), 974-1002. <https://doi.org/10.1785/BSSA0840040974>

930 Weng, H., & Ampuero, J.-P. (2019). The dynamics of elongated earthquake ruptures. *Journal of*
 931 *Geophysical Research: Solid Earth*, 124, 8584–8610. <https://doi.org/10.1029/2019JB017684>

932 Wesnousky, S. G. (2006). Predicting the endpoints of earthquake ruptures. *Nature*, 444(7117),
 933 358-360. <https://doi.org/10.1038/nature05275>

934 Wu, Z. (2022). Seismic Experimental Sites: Challenges and Opportunities. In: Li, Y.G., Zhang,
 935 Y., Wu, Z. (eds) *China Seismic Experimental Site*. Springer, Singapore.
 936 https://doi.org/10.1007/978-981-16-8607-8_1

937 Wu, S., Yao, J., Wei, S., Hubbard, J., Wang, Y., Htwe, Y.M.M., Thant, M., Wang, X., Wang, K.,
 938 Liu, T. & Liu, Q. (2021). New insights into the structural heterogeneity and geodynamics of the
 939 Indo-Burma subduction zone from ambient noise tomography. *Earth and Planetary Science*
 940 *Letters*, 562, 116856. <https://doi.org/10.1016/j.epsl.2021.116856>

941 Xiong, X., B. Shan, Y. M. Zhou, S. J. Wei, Y. D. Li, R. J. Wang, & Y. Zheng (2017), Coulomb
 942 stress transfer and accumulation on the Sagaing Fault, Myanmar, over the past 110 years and its
 943 implications for seismic hazard, *Geophys. Res. Lett.*, 44, 4781–4789,
 944 doi:10.1002/2017GL072770.

945 Xu, L., Mohanna, S., Meng, L., Ji, C., Ampuero, J.P., Yunjun, Z., Hasnain, M., Chu, R. & Liang,
 946 C. (2023). The overall-subshear and multi-segment rupture of the 2023 Mw7. 8 Kahramanmaraş,
 947 Turkey earthquake in millennia supercycle. *Communications Earth & Environment*, 4(1), 379.
 948 <https://doi.org/10.1038/s43247-023-01030-x>

949 Xu, L., Meng, L., Zhang, Y. et al. (2025). Bimaterial Effect and Favorable Energy Ratio Enable
 950 Supershear Rupture in the 2025 Myanmar Quake, submitted.

951 Xu, J., Zhang, H., & Chen, X. (2015). Rupture phase diagrams for a planar fault in 3-D full-
 952 space and half-space. *Geophysical Journal International*, 202(3), 2194-2206.
 953 <https://doi.org/10.1093/gji/ggv284>

954 Yao, D., C. Ding, Z. Peng, E. Sandvol, T. Godoladze and G. Yetermishli (2024), Dynamically
 955 Triggered Tectonic Tremors and Earthquakes in the Caucasian Region Following the 2023
 956 Kahramanmaraş, Türkiye, Earthquake Sequence, *Geophys. Res. Lett.*, 51, e2024GL110786.
 957 <https://doi.org/10.1029/2024GL110786>.

958 Yao, J., Wu, S., Li, T., Bai, Y., Xiao, X., Hubbard, J., Wang, Y., Thant, M. and Tong, P. (2022).
 959 Imaging the Upper 10 km Crustal Shear-Wave Velocity Structure of Central Myanmar via a
 960 Joint Inversion of P-Wave Polarizations and Receiver Functions, *Seismol. Res. Lett.* 93, 1710–
 961 1720, doi: 10.1785/0220210292.

962 Yao, S., & Yang, H. (2025). Rupture phases reveal geometry-related rupture propagation in a
 963 natural earthquake. *Science Advances*, 11(4), eadq0154. <https://doi.org/10.1126/sciadv.adq0154>

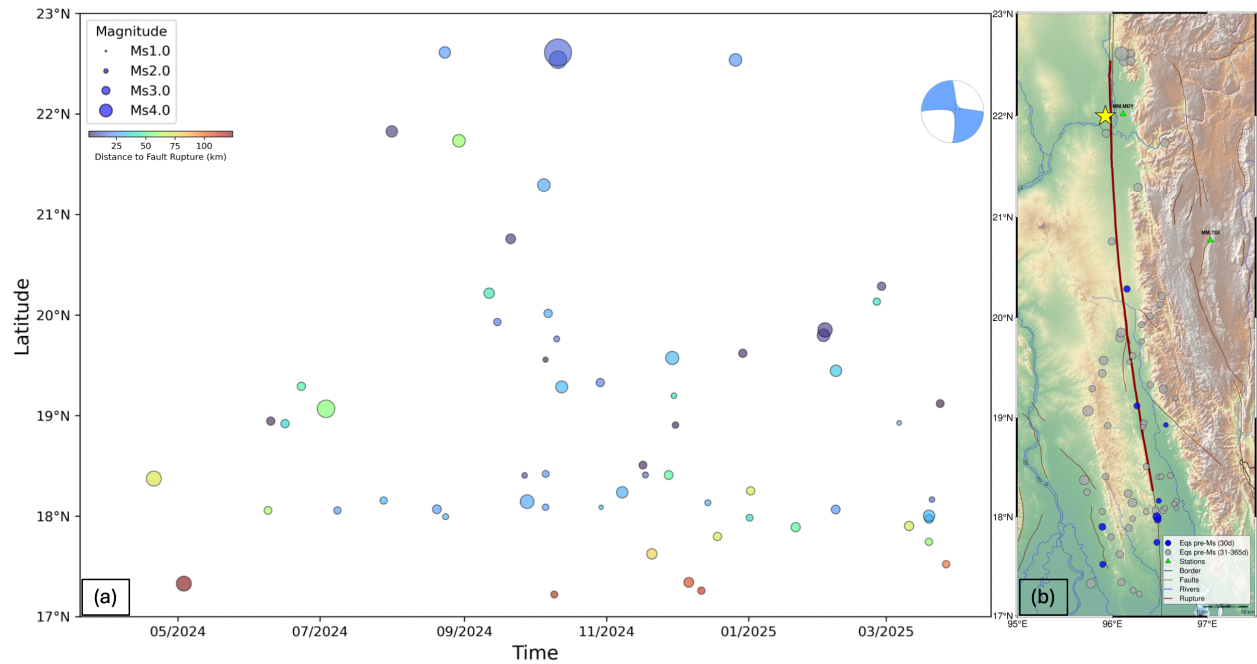
964 Yin, A., & Harrison, T. M. (2000). Geologic evolution of the Himalayan-Tibetan orogen. *Annual*
 965 *review of earth and planetary sciences*, 28(1), 211-280.
 966 <https://doi.org/10.1146/annurev.earth.28.1.211>

967 Yu, Z. & Wang, W. (2022). FastLink: a machine learning and GPU-based fast phase association
 968 method and its application to Yangbi Ms 6.4 aftershock sequences, *Geophysical Journal*
 969 *International*, 230(1), 673–683, <https://doi.org/10.1093/gji/ggac088>

970 Yun, J., Gabriel, A. A., May, D. A., & Fialko, Y. (2025). Controls of Dynamic and Static Stress
 971 Changes and Aseismic Slip on Delayed Earthquake Triggering in Rate-and-State Simulations of
 972 the 2019 Ridgecrest Earthquake Sequence, *J. Geophys. Res.*, in review,
 973 <https://doi.org/10.31223/X55983>

974 Zhao, X. and Meng, L. Peng, G. & He, X. (2025). Aftershock Evolution Characteristics of the 28
 975 March 2025 Mw7.7 Myanmar Earthquake Sequence. *Earthquake Sciences*, in review,
 976 <http://dx.doi.org/10.2139/ssrn.5253293>

977 Zor, E., Z. Peng, M. Ergin, E. Sandvol, F. Sevim, M. C. Tapırdamaz, P. Mach, O. Yalvaç, A.
 978 Tarancioğlu, M. K. Koşma, O. Adeboboye, C. Ding, C. Açıkgöz, and E. Büyük (2025), Dense
 979 Seismic Recordings of the 2023 Kahramanmaraş Earthquake Sequence in Southeastern Türkiye.
 980 *Seismol. Res. Lett.*, <https://doi.org/10.1785/0220240152>
 981



Supplementary Figure 1: Earthquakes recorded along the fault rupture zone one year before the M7.7 Sagaing earthquake mainshock. (a) Latitudes versus occurrence times for earthquakes near Sagaing fault recorded based on TMD catalog one year before the mainshock. (b) The location map view of the earthquakes one year before the mainshock.

Supplementary Table: Catalog of earthquakes 3 hours after the Sagaing mainshock. For Original Catalog: U for USGS, T for TMD, and E for EMSC. Potential overlapping events in three catalogs are highlighted alternatively in blue and yellow.

Datetime (UTC)	Latitude	Longitude	Depth	Magnitude	Magnitude Type	Original Catalog
2025-03-28 06:20:52.709	22.0014	95.9247	10.0	7.7	mww	U
2025-03-28 06:20:54.000	21.991	95.935	10.0	7.7	Mw	E
2025-03-28 06:20:55.000	21.682	96.121	10.0	8.2	Ms	T
2025-03-28 06:32:04.777	21.6975	95.969	10.0	6.7	mww	U
2025-03-28 06:32:05.000	21.759	95.991	10.0	6.7	Mw	E
2025-03-28 06:32:10.000	21.415	96.383	10.0	7.1	Ms	T
2025-03-28 06:39:15.000	19.971	95.821	10.0	4.8	mb	E
2025-03-28 06:39:15.041	19.9711	95.8212	10.0	4.8	mb	U
2025-03-28 06:42:24.000	21.898	95.837	10.0	4.9	mb	E
2025-03-28 06:42:24.866	21.898	95.8365	10.0	4.9	mb	U
2025-03-28 06:45:44.000	19.17	96.254	10.0	5.5	Ms	T
2025-03-28 06:45:45.000	19.244	96.3	13.0	4.9	mb	E
2025-03-28 06:45:45.503	19.3005	96.2925	10.0	4.9	mb	U
2025-03-28 06:54:31.000	18.037	96.512	10.0	4.4	Ms	T
2025-03-28 06:57:53.711	22.0976	96.0667	10.0	4.5	mb	U
2025-03-28 07:01:28.860	22.0534	95.8669	10.0	4.4	mb	U
2025-03-28 07:24:25.000	18.697	96.871	10.0	4.0	Ms	T

2025-03-28 07:27:47.000	22.684	95.769	10.0	4.6	mb	E
2025-03-28 07:27:47.947	22.7236	95.8606	10.0	4.6	mb	U
2025-03-28 07:33:00.000	25.57	90.58	5.0	4.0	M	E
2025-03-28 07:33:37.000	22.647	95.775	10.0	4.4	mb	E
2025-03-28 07:33:37.783	22.628	95.7357	10.0	4.4	mb	U
2025-03-28 07:36:58.000	22.769	95.895	10.0	4.6	mb	E
2025-03-28 07:36:58.799	22.7673	95.8531	10.0	4.6	mb	U
2025-03-28 07:37:16.000	21.767	96.696	10.0	5.2	Ms	T
2025-03-28 07:42:36.000	20.022	96.863	10.0	4.3	mb	E
2025-03-28 07:42:37.052	20.0771	96.9762	10.0	4.3	mb	U
2025-03-28 07:42:42.000	18.549	96.716	10.0	3.9	Ms	T
2025-03-28 07:49:21.000	19.527	98.547	3.0	3.3	Ms	T
2025-03-28 07:50:43.000	18.967	96.416	10.0	3.5	Ms	T
2025-03-28 07:57:00.000	22.479	95.876	10.0	4.5	mb	E
2025-03-28 07:57:00.754	22.5423	95.8338	10.0	4.5	mb	U
2025-03-28 07:57:07.000	21.552	96.337	10.0	4.7	Ms	T
2025-03-28 07:59:08.865	22.2037	96.117	10.0	4.3	mb	U
2025-03-28 07:59:55.000	24.96	94.69	10.0	4.3	M	E
2025-03-28 08:21:22.000	18.77	96.608	10.0	4.0	M	E
2025-03-28 08:21:22.000	18.77	96.608	10.0	4.0	Ms	T

2025-03-28 08:33:16.920	6.4042	124.5678	10.0	4.2	mb	U
2025-03-28 08:33:17.000	6.68	124.57	10.0	3.5	M	E
2025-03-28 08:45:57.000	19.366	96.389	10.0	3.7	Ms	T
2025-03-28 08:45:57.000	19.366	96.389	10.0	3.7	M	E
2025-03-28 08:52:00.000	19.007	96.518	10.0	3.8	M	E
2025-03-28 08:52:00.000	19.007	96.518	10.0	3.8	Ms	T
2025-03-28 09:06:18.000	20.769	96.469	10.0	4.2	M	E
2025-03-28 09:06:18.000	20.769	96.469	10.0	4.2	Ms	T
2025-03-28 09:11:46.000	19.925	96.377	10.0	3.8	M	E
2025-03-28 09:11:46.000	19.925	96.377	10.0	3.8	Ms	T
2025-03-28 09:18:13.000	19.531	98.551	1.0	3.1	Ms	T
2025-03-28 09:18:28.000	23.522	95.37	10.0	4.4	mb	E
2025-03-28 09:18:28.345	23.5224	95.3699	10.0	4.4	mb	U
2025-03-28 09:26:46.000	21.639	97.7	10.0	4.1	mb	E
2025-03-28 09:26:46.362	21.6385	97.7004	10.0	4.1	mb	U
2025-03-28 09:26:47.000	19.857	96.332	10.0	4.3	Ms	T